The importance of wind turbulence and coherence to the loads on a wind turbine blade

Master Thesis in Renewable Energy

by

Phani Kumar Manne

University of Bergen
Faculty of Mathematics and Natural Sciences
Geophysical Institute

June 2019

Abstract

The wind simulation method proposed by Paul S. Veers from Sandia National Laboratories has been checked for the measured wind velocities at 40m and 80m height at FINO1 platform. The Sandia method applied as it is, gives relatively higher standard deviation (turbulence) than the actual but works better when random phases are used. A code for the generation of wind field based on Sandia method has been developed from a time series of wind speed at hub center. Various wind fields based on difference in wind shear and turbulence intensity have been projected on to the reference wind turbine to find root bending moments of the blade. The bending moments are calculated based on 2D Beam Element Momentum theory. The mean bending moment values are affected by wind shear while the maximum bending moments by turbulent intensity. An increase in turbulence in the wind field will increase the maximum and standard deviation of flap-wise bending moment drastically.

Acknowledgements

Contents

List of Figures

List of Tables

1   Introduction

In the design of wind turbines, wind data is needed to extract power and to estimate the loads on the turbine blades. Wind data is available either from site measurements or from wind models. In offshore wind, very few site measurements are available because the costs to establish and maintain an offshore wind measuring platform are very high. So, theoretical wind models are generally preferred to generate wind field data.

A wind field can be generated by using Sandia (Veers) method (8) or Jakob Mann method (9). It contains information about mean wind and turbulent wind speeds. A wind field can be imagined as a box with known amplitudes and direction of wind at various points in the atmosphere. In practice, this box is projected onto the wind turbine with a mean wind speed assuming Taylor's frozen turbulence hypothesis. From the view point of the rotor plane, it can be seen as a time series of velocities passing through.

These time series are coherent to each other. Coherence decreases with increasing separation distance. Modelling correct coherence in the generation of wind field is very important. Various coherence models exist in the literature (10). The theoretical coherence models only provide the magnitude of the coherence but does not contain information about phase angles. The phase angles are often neglected because the quad-spectrum is often assumed small for small separation distances in a homogeneous turbulence field. These conditions are not always met and phase angles could be high and relevant. This has been observed at Høvsøre test site for vertical separation distances (11).

The importance of phase angles in the generation of wind field has been investigated in the first half of the thesis. Sandia method is chosen as wind field generation method. First, simple time series with combination of 3 different cosine functions with different phase angles is looked at. Next, measured wind data at 40m and 80m height at FINO1 station in neutral atmospheric conditions is investigated. Various cases have been considered based on how and what to use for phase angles so that time series at 80m height can be reproduced statistically based only on the information from time series at 40m height. Once, a procedure has been finalized, computational code to generate the whole wind field box based on Sandia method has been developed. A new code has also been written to generate a wind field in cylindrical co-ordinates rather than a rectangular wind field for added benefits.

Once a turbulent wind field is generated, it can be used to find structural loads on the wind turbine. Global structural loads, flap-wise and edge-wise root bending moments of the blade are calculated based on 2D Beam Element Momentum (BEM) theory. Various cases are established based on the difference in wind shear and turbulent intensity in the generated wind field and the effect of these on root bending moments have been investigated.

2 Background theories and methods

2.1 Taylor's frozen turbulence hypothesis

Taylor's hypothesis assumes that the turbulence is frozen while the wind is advected over the rotor blade. This means that, once a wind field is generated, the properties of it won't change until it passes through the wind turbine. This assumption is only valid under some specific conditions. One of the conditions is that the time required for the wind field to advect past the turbine is less the time required for turbulent eddies to evolve. This condition is hard to meet when large wind fields are considered. Other condition is to have the turbulence intensity over mean wind speed to be under 0.5. This implies, Taylor's hypothesis can only be used on the wind field generated numerically if turbulence intensity is kept below 50%. From the wind data collected at FINO1 station located in the North Sea, it has been observed that the turbulence intensity is around 10%. The same is used in this thesis. Taylor's hypothesis converts the spacial domain data to time domain and vice versa (1).

$$\frac{\partial \theta}{\partial t} = -U \frac{\partial \theta}{\partial x} \tag{1}$$

Where,
U = mean wind velocity in x-direction
θ = any turbulent parameter

Fig. 1.4 Illustration of Taylor's hypothesis. (a) An eddy that is 100 m in diameter has a 5 ° C temperature difference across it. (b) The same eddy 10 seconds later is blown downwind at a wind speed of 10 m/s.
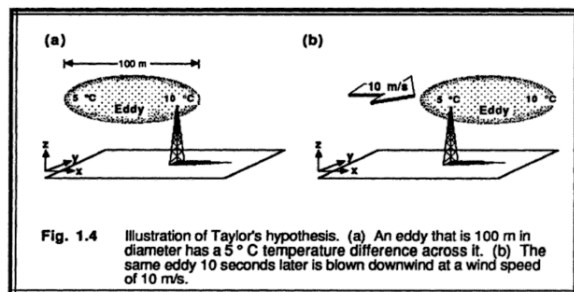
Figure 1: Plot showing how Taylor's hypothesis works (1)

2.2 Atmospheric stability

The atmospheric stability tells us how easy it is for an air parcel to move vertically in the atmosphere. In an unstable atmospheric condition, once an air parcel is disturbed form it's location, it keeps on moving away. Turbulence is high in these conditions. In a stable atmosphere, the parcel returns to it's original location. Turbulence is low in this condition. In a neutral atmosphere, an air parcel moved from it's location will stay at a new location. It will neither move back to it's original location nor away. Turbulence is moderate in this condition.

Atmospheric condition plays a vital role in defining the turbulence and also mean wind profile. For Taylor's hypothesis to be valid, neutral atmospheric stability should be present. The measured data taken for analysis is for neutral condition. The mean wind profile in neutral atmospheric stability is gives as:

$$U(z) = U_{ref} \frac{\ln(\frac{z}{z_0})}{\ln(\frac{z_{ref}}{z_0})} \qquad (2)$$

Where,
$U(z)$ = mean wind velocity in x-direction at a certain height
U_{ref} = mean wind velocity known at a certain reference height
z = height above ground level
z_0 = roughness length (depends on the site)
z_{ref} = reference height

2.3 Coherence

Winds at different horizontal and vertical separations in the atmosphere are not independent of each other. Some correlation exists between them. Coherence is a measure of this correlation in frequency domain. The magnitude of coherence depends on the separation distance, mean wind speed and frequency. The higher the separation distance, the lesser coherence between them. It also decreases exponentially with frequency.

Coherence between two points in the atmosphere is described as the normalized cross-spectrum between time series of turbulent wind velocities at these points. These are complex value numbers at different frequencies. The real part of the spectrum is called co-coherence where as the imaginary part is called quad-coherence. There are different ways of defining the coherence in the literature. Some simply refer the co-coherence as coherence and others the magnitude square of normalized cross spectrum. In this thesis, only the coherence in the along wind direction (uu-coherence) for lateral and vertical separations is considered and the coherence is defined either as the square root of the magnitude square of normalized cross spectrum called "Magnitude coherence" or just the "Co-coherence" as coherence whenever applied. It is chosen like this because, a complex normalized cross-spectrum can be represented in the polar form as:

$$x + iy = |a|e^{i\theta} \qquad (3)$$

Where,
x = Co-coherence
$a = \sqrt{x^2 + y^2}$ Magnitude coherence
$\theta = \arctan(\frac{quad-coherence}{co-coherence})$ Phase angle

2.4 Sandia method

In the wind industry, Sandia method (8) is used for generating a three dimensional field of turbulent wind speeds numerically which is used for aerodynamic and structural analysis of wind turbines. The method requires single point power spectral densities and coherence functions as input. The output will be time series of turbulent wind speeds at these points. Sandia method is based on a mathematical method developed by Shinozuka (12).

Let's say time series at N number of points in the plane perpendicular to mean wind speed are needed. Sandia method creates these N correlated time series based on a spectral matrix $\boldsymbol{S}$. This spectral matrix is symmetrical with dimensions NxN. The diagonal of $\boldsymbol{S}$ contains auto spectra of the N points and off-diagonal terms contain cross spectra. Cross spectrum between two points j and k can be calculated based on the coherence function and auto spectra of these two points.

$$\mid S_{jk}(f_m)\mid = Coh_{jk}(f_m, r_{jk}, U_{jk})\sqrt{S_{jj}(f_m)S_{kk}(f_m)} \tag{4}$$

Where,
$S_{jk}(f_m)$ is the cross spectrum at frequency f_m
$S_{jj}(f_m)$ is the auto spectrum for point j at frequency f_m
$S_{kk}(f_m)$ is the auto spectrum for point k at frequency f_m
Coh_{jk} is the coherence function which depends on frequency f_m, distance between j and k, r_{jk} and average of mean wind velocities U_j and U_k, U_{jk}

A lot of coherence functions exist in the literature. In this thesis, coherence function suggested by Frost (13) is used. This is a real value function. It means the cross spectra won't have any imaginary components. So, this comes with a preliminary assumption that the average phase difference between any two points is zero. However this is not a real scenario. Phase lag can exist between points of various heights because of wind shear. Nevertheless, Frost coherence function is often used along with Sandia method and given as:

$$Coh_{jk} = exp\left(-\frac{C\ r_{jk}\ f_m}{U_{jk}}\right) \tag{5}$$

C is the exponential decay parameter or also called coherence decrement. Lot of experiments have been made to get an proper estimate for the value of C. Any value between 2 to 27 has be suggested. But, Frost recommended the value of 7.5 for lateral spacing. The same value has been used in this thesis in all of the wind field irrespective of the direction for simplicity.

Now the spectral matrix $\boldsymbol{S}$ can be found based on coherence functions and auto spectra. $\boldsymbol{S}$ can also be written in terms of a transformation matrix $\boldsymbol{H}$ and the transpose of it's complex conjugate.

$$\boldsymbol{S}(f_m) = \boldsymbol{H}(f_m)\boldsymbol{H^{*T}}(f_m) \tag{6}$$

Since S is a real matrix, H must also be real. The transformation matrix H is not uniquely defined though. However, if H is assumed to be a lower triangular matrix, the non-zero values can be uniquely defined in a recursive operation starting with k=1 and j=2 as:

$$H_{kk} = \left(S_{kk} - \sum_{l=1}^{k-1} H_{kl}^2\right)^{1/2}$$

$$H_{jk} = \frac{\left(S_{jk} - \sum_{l=1}^{k-1} H_{jl}H_{kl}\right)}{H_{kk}}$$

(7)

The elements in each row of H gives the input for the formation of time series of wind velocities at a point k along with phase angles which are generated randomly by a uniformly distributed variable at the interval $[0\ 2\pi]$. The phase matrix X is given as:

$$X_{kk}(f_m) = e^{i\theta_{km}}$$

(8)

Where θ_{km} is the phase angle for a point k at frequency m. The Fourier coefficients matrix of the wind velocities V can be found from H and X. Each element of matrix V is given as:

$$V_j(f_m) = \sum_{k=1}^{j} H_{jk}(f_m)e^{i\theta_{km}}$$

(9)

The inverse Fourier transform of V gives the time series of wind velocities for all N points.

Let's see how the method actually works. Say we want to find time series of wind velocities at 2 different points in the atmosphere. The input needed for the method is auto spectrum at point 1 and 2 (S_{11} and S_{22}) and the coherence function (Coh_{12}). The cross spectrum between 1 and 2 can be found from equation 4 as,

$$S_{12} = Coh_{12}\sqrt{S_{11}S_{22}}$$

The spectral matrix S is now known[1].

$$S = \begin{bmatrix} S_{11} & S_{12} \\ S_{21} & S_{22} \end{bmatrix}$$

The transformation matrix H can be found based on S. The elements of H from equation 7 are given as,

$$H_{11} = S_{11}^{1/2}$$
$$H_{21} = S_{21}/H_{11}$$
$$H_{22} = (S_{21} - H_{21}^2)^{1/2}$$

---

[1]$S_{12} = S_{21}$

so that the lower triangular matrix $\boldsymbol{H}$ is,

$$\boldsymbol{H} = \begin{bmatrix} H_{11} & 0 \\ H_{21} & H_{22} \end{bmatrix}$$

The phase angles at point 1 and 2 can be generated from a uniformly distributed random variable between $[0\ 2\pi]$ as θ_1 and θ_2. The elements of Fourier coefficient matrix $\boldsymbol{V}$ can be found from equation 9 as,

$$V_1 = H_{11}e^{i\theta_1}$$
$$V_2 = H_{21}e^{i\theta_1} + H_{22}e^{i\theta_2}$$

The real values of inverse Fourier transformation (ifft) of V_1 gives the times series of wind velocities at point 1 because the terms of H_{11} and θ_1 correspond to the Fourier amplitudes and it's phases at different frequencies and the phases due to time $(\omega_1 t)$ will be included while performing ifft. Similarly, ifft of V_2 gives the time series of wind velocities at point 2.

2.5   DTU 10MW HAWT

The reference turbine used to find structural loads based on the wind field generated by Sandia method is DTU 10MW Horizontal Axis Wind Turbine (HAWT). The main characteristics of the turbine that are useful for this thesis are listed below. More details of the turbine can be found in (7).

- Rated wind power, 10MW

- No. of blades, 3

- Hub height, 119m

- Hub diameter, 5.6m

- Rotor diamater, 178.3m

- Cut-in wind speed, 4m/s

- Rated wind speed, 11.4m/s

- Cut-out wind speed, 25m/s

- Cut-in rotor speed, 6rpm

- Rated rotor speed, 9.6rpm
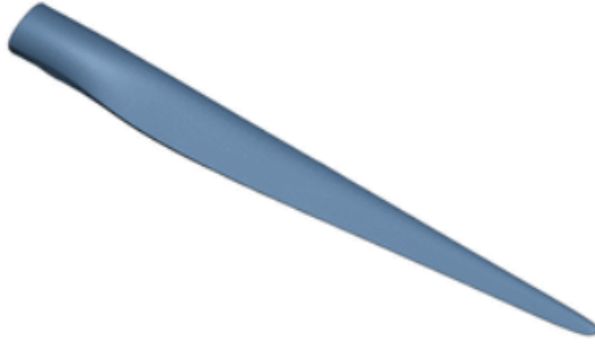
Figure 2: Plot of the blade of DTU 10MW reference turbine (2)

Figure 2 shows the shape of the blade for the reference wind turbine. Structural loads are calculated at the root of this blade. An efficient wind turbine blade contains different airfoil types over the span with a twist angle. The blades of DTU 10MW HAWT contains 5 different airfoils of type FFA-W3-xxx. The values in xxx gives information about the relative thickness of the airfoils. Five different relative thickness of 60%, 48%, 36%, 30.1% and 24.1% are used with 60% being close to the root and 24.1% close to the tip. The root of the blade and 60% relative thickness airfoil are connected by a cylinder which in airfoil terms, an 100% relative thickness airfoil which can't produce any lift but just drag. The aerodynamic properties of various airfoils of the blade can be found in (7).
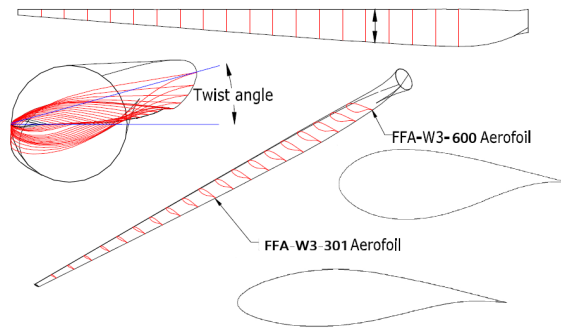
Figure 3: Plot of sections of the blade with various airfoil types (3)

The mass of each blade is 41,716 kg with center of gravity located at 26.2m along the span from the root. In the present work, no pre-bend, shaft-tilt and pre-coning is considered while calculating structural loads.

2.6   2D Blade Element Momentum (BEM) theory

BEM theory combines the momentum theory and blade element theory. It is used to find local forces on each element which can be combined together to find total forces acting on the rotor. Each element of the blade is considered as a 2D airfoil, see figure 3. No interactions between elements is considered and steady flow is assumed. Experiments might be needed to find lift and drag coefficients of the airfoils for various angles of attack. Once the lift and drag coefficients are established, lift and drag forces can be found for relevant angle of attack. Using these lift and drag forces, thrust and torque on each element and on the whole rotor can be found.

Figure 4 shows the nomenclature of an 2D airfoil. The angle of attack, α is the angle between incoming flow and chord line. Figure 5 shows velocities at rotor plane and how α can be calculated based on local wind and rotational speeds along with axial and angular induction factors.
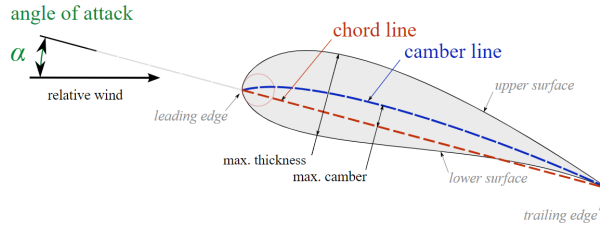
Figure 4: Plot of 2D airfoil (4)
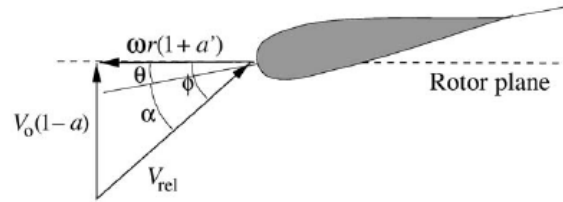
Figure 5: Plot showing the velocities experiences by blade element/airfoil on rotor plane (5)

The wind velocity V_0 is perpendicular to the rotor plane while the local rotational velocity ωr is in the rotor plane. The actual velocity experienced by the airfoil is V_{rel}.

$$V_{rel} = \sqrt{[V_0(1 - a)]^2 + [\omega r(1 + a')]^2} \tag{10}$$

$$\phi = \arctan \frac{V_0(1 - a)}{\omega r(1 + a')} \tag{11}$$

16

The angle of attack, α is given as $\phi - \theta$. θ is found from blade's local twist angle, pitch of the blade and local deformations. The pitch of the blade for below rated wind speed will be zero and then increases with increasing wind speed. No local deformations are taken into account assuming a stiff blade. Once α is known, the lift and drag coefficients (C_l, C_d) can be extracted to find lift and drag forces on the airfoil (L, D).

$$L = \frac{1}{2}\rho A V_{rel}^2 C_l$$
$$D = \frac{1}{2}\rho A V_{rel}^2 C_d \tag{12}$$

where,
ρ is the density of the air
A is the area of the element which is the product of chord length and element size
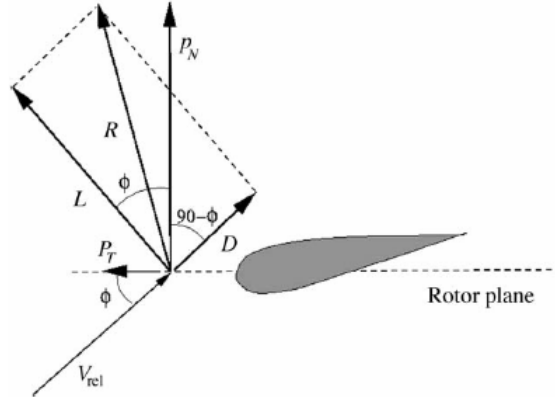
Figure 6: Plot showing the loads on the blade element (5)

The lift force (L) will be perpendicular to the incoming velocity V_{rel} and drag force (D) will be parallel. Using L, D, ϕ, the force normal to the rotor plane (P_N) and tangential to the rotor plane (P_T) can be calculated.

$$P_N = L cos\phi + D sin\phi$$
$$P_T = L sin\phi - D cos\phi \tag{13}$$

P_N is the thrust on the blade element and P_T is the force that is driving the rotation. P_T multiplied by local radius gives local torque. Combining thrust and torque of all the elements of 3 blades gives total thrust (T) and torque (Q) on the rotor plane. The torque multiplied by angular velocity (ω) gives the power output of the turbine $(P = \omega Q)$.

The axial and angular induction factors, a and a' plays a major role in determining the output power. Some iterations are needed to find proper a and a'. The iterations are initialized

17

with $a = 0$ and $a' = 0$. First, the flow angle ϕ is computed from equation 11 and then the angle of attack, α. The lift and drag coefficients, C_l and C_d are read for corresponding α. From C_l and C_d, the lift and drag forces, L and D are calculated from equation 12. From L and D, the thrust, P_N and torque, Q can be calculated from equation 13. This P_N and Q will then be equated to the thrust and torque from momentum theory to find new a and a'. This process is repeated until a and a' hasn't changed more than a certain tolerance.

When operating at above rated wind speed with power output of 10MW, a' will be close to zero. The wind field generated in order to find loads on the blade is an above rated mean wind speed. So, a' is kept at zero for simplicity. The corrections for BEM theory like Prandtl's tip loss factor, Glauert's limit ($a > 0.4$) and 3D effects are not applied in this thesis.
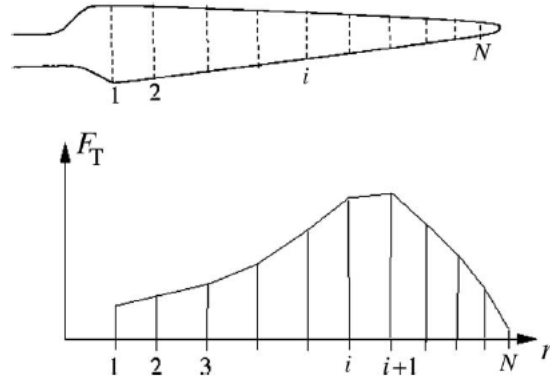
Figure 7: Plot showing the thrust forces along the blade by assuming a linear variation between elements (5)

2.7 Root bending moments

Depending on the bending plane, there are two different types of bending moments at the root of the blade, Flap-wise and Edge-wise. No structural deflections are considered while calculating root bending moments.

2.7.1 Flap-wise bending moment

The forces that are normal to the rotor plane, P_N contribute to the flap-wise bending moment. The bending occurs about the chord axis of the airfoils creating tensile and compressive stresses across blade cross section.
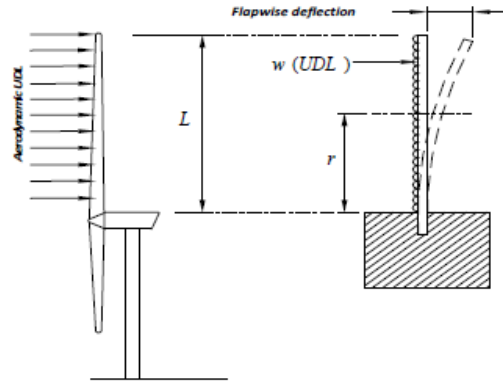
Figure 8: Plot showing normal loads and flap-wise bending (3)

2.7.2 Edge-wise bending moment

The forces that act in the rotor plane like P_T and gravitational forces contribute to the edge-wise bending moment. The plane of bending is normal to the chord line axis of the airfoils of the blade. The bending moment due to gravity is the main component of edge-wise bending moment. The maximum edge-wise bending moment occurs when the blade reaches horizontal position as the bending moment due to gravity will be high.
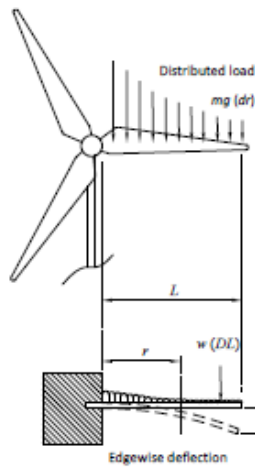
Figure 9: Plot showing gravitational loads and edge-wise bending (3)

2.8 Fourier analysis in MATLAB

Understanding Fourier analysis is very important while dealing with spectra. Fourier analysis can be done by using FFT (Fast Fourier Transform) or PSD (Power Spectral density) functions in MATLAB (same as periodogram).

Let's take a time series of length, N and total time, T for investigation. FFT of the time series gives an output of complex amplitudes and it's phase angles at different frequencies of interval 1/T. The complex amplitudes have to be normalized by N in order to continue with further calculations. This is because, MATLAB by default performs FFT by multiplying the time series with its length.

By the spectral density approach, the periodogram produced by default is a one-sided spectrum. This means the values of the periodogram are doubled at each frequency except at zero and Nyquist frequency. Also, the PSD values should be multiplied with N and sampling frequency in order to take care of the scaling. The amplitudes at each frequency are then obtained from the square root of these values. This approach uses less computational time than FFT to generate the time series back from the calculated amplitudes and phases and therefore adopted to rest of the thesis.

2.9 Wind field generation by Sandia method

Sandia method is used to generate a whole wind field based on a initial input time series $(x(t))$ at a single point. The time series at a different location $(y(t))$ can be found based on the auto-spectrum of $x(t)$, theoretical coherence function, phase angles as obtained by the FFT of $x(t)$ and randomly generated phases for $y(t)$. A different time series at a different location can be generated by following the same procedure but now with the information from both $x(t)$ and $y(t)$ and so on until the whole field is generated.

2.9.1 Sandia method on regular signals

The procedure as described in section 2.4 has been applied on two known signals (combinations of 3 sinusoidal functions) to get a feel on how the method actually works. The signals or time series are taken as,

$$x(t) = 1 * cos(2\pi t) + 2 * cos(4\pi t + \pi/4) + 1 * cos(6\pi t + \pi/2)$$
$$y(t) = 2 * cos(2\pi t + \pi/4) + 1 * cos(4\pi t + \pi/2) + 2 * cos(6\pi t)$$

where,
t $= 0 : \Delta t :$ T

The time step, Δt is assumed to be 0.01 seconds and total time, T = 10.24 seconds. This gives the number of discrete points or time steps, N to be 1024. The number of discrete points has to be 2^n for the PSD algorithm to work properly in MATLAB.

The auto spectra, coherence and phase angles that are needed for Sandia method are calculated from above $x(t)$ and $y(t)$. The procedure is followed as described to generate new time series $x_{new}(t)$ and $y_{new}(t)$. These new time series from Sandia method are compared with original time series $x(t)$ and $y(t)$. The time series $x(t)$ can be reproduced exactly but not $y(t)$.
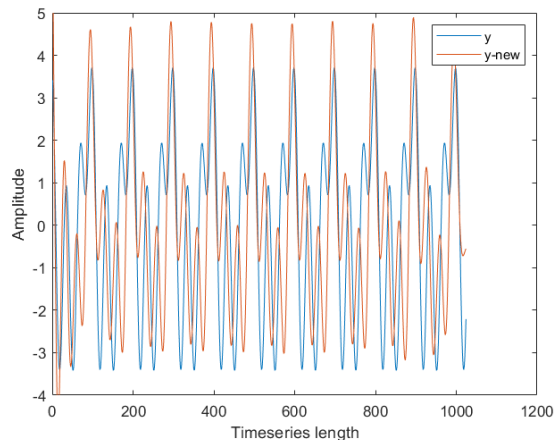
Figure 10: Plot of $y(t)$ and $y_{new}(t)$ generated by following Sandia method

It has been observed that, Sandia method as it is applied can conserve the statistics of the signal but not the shape. The mean and standard deviation of $y(t)$ is -0.02 and 2.13. While, the mean and standard deviation of $y_{new}(t)$ is -0.06 and 2.17.

If the shape of $y_{new}(t)$ should coincide with $y(t)$, a slight modification is needed where phase angles of $y(t)$ has to be used at element H_{21} of lower triangular matrix instead of phase angles of $x(t)$ while re-generating time series $y(t)$. The mean and standard deviation in this case came out to be -0.06 and 2.19. The mean is the same while there is a slight increase in standard deviation but the shape can be generated back except at ends. Figure 11 shows the signals $y(t)$ and $y_{new}(t)$ for the modified method.
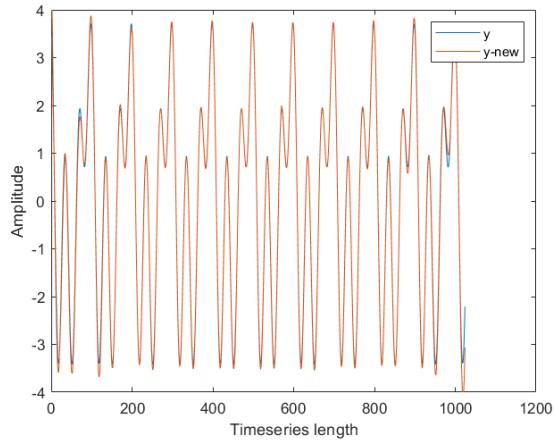
Figure 11: Plot of $y(t)$ and $y_{new}(t)$ generated by using phase angles of $y(t)$ at H_{21}

Figure 12 shows the auto spectrum of $y(t)$, P_{yy} and $y_{new}(t)$, $P_{yy}new$ for the modified method. They are almost identical.
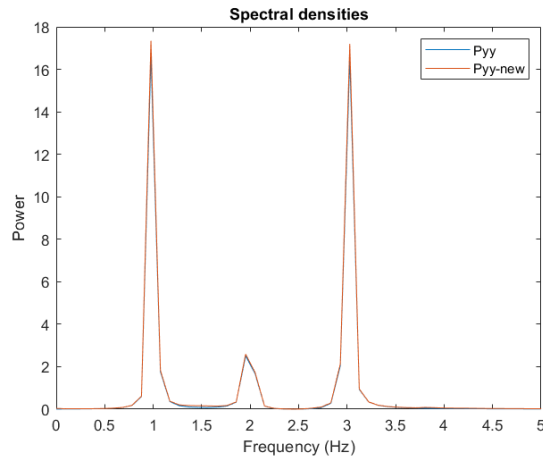
Figure 12: Plot of spectral densities of $y(t)$ and $y_{new}(t)$

3 Results and discussions

3.1 Sandia method on measured signals

In this section, it is investigated whether Sandia method can be used to reproduce measured signals. Measured wind data from FINO1 station at 40m and 80m height under neutral conditions is selected (14). The length of the time series is 76000 steps with frequency 20Hz. This gives a total measuring time of over 1 hour. Mean is taken out of the time series and only turbulent part is preserved.

Five different cases of the method have been looked at based on spectra, phase angles and coherence of the measured signals. It is investigated if time series at 80m height can be reproduced by using the information only from time series at 40m eventually.

Case 1: Original Sandia method. Spectrum, coherence and phase angles are calculated from the measured signals and used accordingly as specified in the method to see if they can be reproduced back.
Case 2: A slightly modified method where only the phase information of the second signal is used to generate it back rather than using phase information from both signals.
Case 3: Phase angles for second signal are generated randomly
Case 4: Random phases of second signal and theoretical coherence function
Case 5: Random phases of second signal, theoretical coherence function and similar spectra

3.1.1 Case study 1

Time series at 40m is taken as initial/first signal $x(t)$. From Fourier analysis of $x(t)$, the spectrum (P_{xx}) and phase angles (phaseX) can be computed at each frequency till Nyquist frequency. Similarly, time series at 80m (second signal) is labelled as $y(t)$ with spectrum as P_{yy} and phase angles as phaseY. The main purpose is now to see if Sandia method can reproduce more or less $x(t)$ and $y(t)$ back if all the input information is known beforehand i.e, information about $x(t)$ and $y(t)$. The newly generated time series are called $x_{new}(t)$ and $y_{new}(t)$.

The coherence function used in the method is the calculated coherence in along wind direction (uu-coherence) between the original time series $x(t)$ and $y(t)$. Mean squared coherence is calculated with 8 Hamming windows and 50% overlap between each window (15). The square root of these values give actual coherence values, named C_{xy}. It should be noted that these coherence values won't approach zero at high frequencies as this is not co-coherence but magnitude of the complex coherence. It will always have values greater than zero.

It is observed that the newly generated time series $x_{new}(t)$ is exactly the same as $x(t)$ as seen in figure 13 because it is just fft and ifft of the time series. But time series $y_{new}(t)$ is bit different from $y(t)$ as seen in figure 14. When followed Sandia method with all the input

from original time series, the standard deviation of the newly generated time series $y_{new}(t)$ is higher than the original time series $y(t)$ but the mean is maintained which is zero. The shape of the original time series is retained in the new time series but the standard deviation has increased by 16%. The below table 1 shows the properties of the time series.

Table 1: Difference in properties of time series $y(t)$ and $y_{new}(t)$

	mean	standard deviation
$y(t)$	$3.3e^{-14}$	1.784
$y_{new}(t)$	$-5.9e^{-14}$	2.069
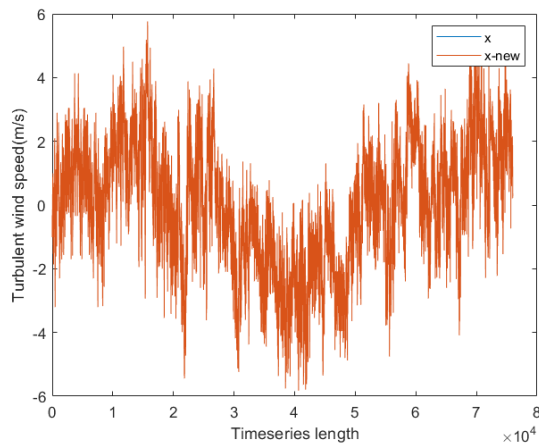
Figure 13: Plot of $x(t)$ and $x_{new}(t)$ generated by following Sandia method
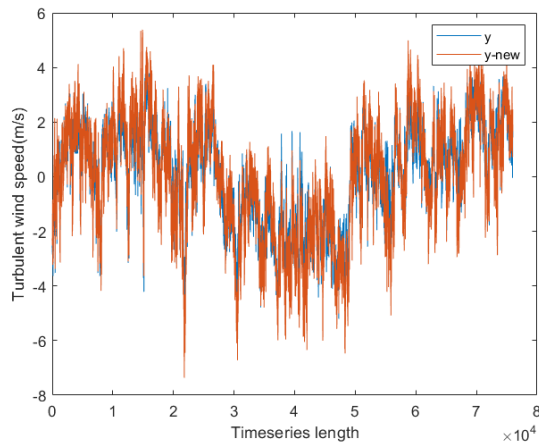
Figure 14: Plot of $y(t)$ and $y_{new}(t)$ generated by following Sandia method

24
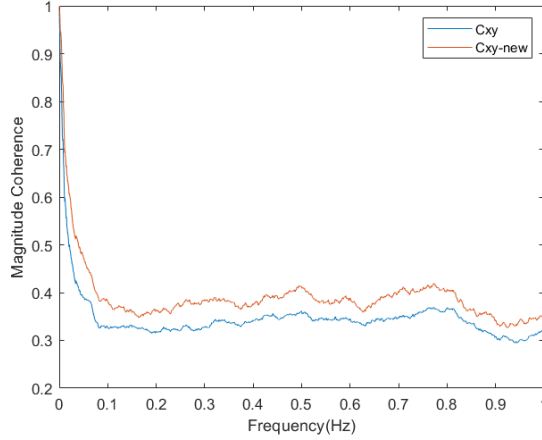
Figure 15: Plot of C_{xy} and $C_{xy}new$

Figure 13 represents the original time series $x(t)$ and generated time series $x_{new}(t)$. They are identical. Figure 14 represents the original time series $y(t)$ and generated time series $y_{new}(t)$. There are some changes in the new time series but follows the original time series pattern. Overall the values seems bit higher and hence higher standard deviation. Figure 15 represents the original coherence between $x(t)$ and $y(t)$, C_{xy} and new coherence between $x_{new}(t)$ and $y_{new}(t)$, $C_{xy}new$. The newly generated coherence $C_{xy}new$ is bit higher than C_{xy} at all frequencies. This is because of the influence of phaseX in generation of $y_{new}(t)$. The cross component H_{21} of lower triangular matrix in Sandia method is multiplied with phaseX and added to the product of H_{22} and phaseY in order to generate $y_{new}(t)$. Therefore phaseX has influence over $y_{new}(t)$ at least at lower frequencies because H_{21} is significantly higher than H_{22}. Therefore higher coherence is expected at lower frequencies. It is also observed that $C_{xy}new$ is higher than C_{xy} in all frequency range but follows a similar pattern.

3.1.2 Case study 2

In order to rectify the coherence, Sandia method is modified and run again. The cross component H_{21} of lower triangular matrix is multiplied with phaseY instead of phaseX. No difference in $x(t)$ and $x_{new}(t)$ is expected and observed. The below figures 16 and 17 and table 2 shows the differences in $y(t)$ and $y_{new}(t)$ for the new run.
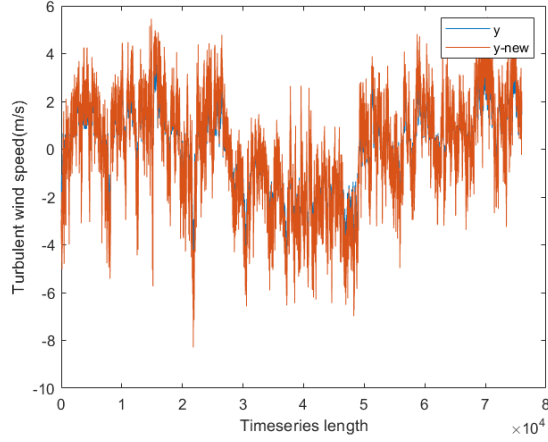
Figure 16: Plot of $y(t)$ and $y_{new}(t)$ with phaseY used at H_{21}
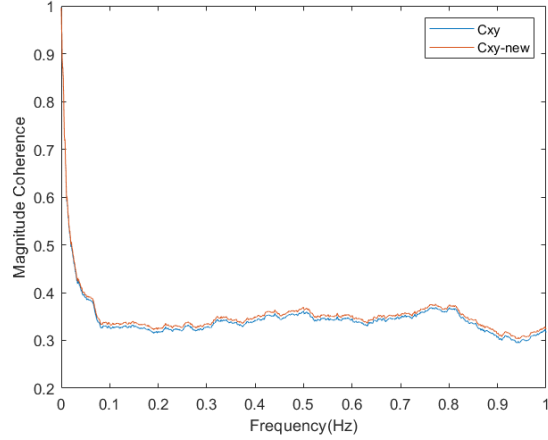
Figure 17: Plot of C_{xy} and $C_{xy}new$ with phaseY used at H_{21}

Table 2: Difference in properties of time series $y(t)$ and $y_{new}(t)$ with phaseY used at H_{21}

	mean	standard deviation
$y(t)$	$3.3e^{-14}$	1.784
$y_{new}(t)$	$6.6e^{-14}$	2.168

It can be seen from figure 16 that generated time series $y_{new}(t)$ follows exactly the pattern of $y(t)$. Even though the pattern is almost identical, $y_{new}(t)$ has higher values than $y(t)$ almost everywhere. That explains the high standard deviation. It should be noted that this standard deviation for $y_{new}(t)$ is even higher than the one from table 1. But, the coherence $C_{xy}new$ is very similar to original coherence C_{xy} which is seen in figure 17. This is because

26

only phaseY is used to generate $y_{new}(t)$. Even though this method produces better coherence than original Sandia method, it increases the standard deviation of the newly generated time series by 22%.

3.1.3 Case study 3

Both cases 1 and 2 have some problems recreating the time series $y(t)$ back. Now, a different approach has been looked at. The original Sandia method is taken again i.e, H_{21} is multiplied with phaseX and H_{22} is multiplied by phaseY and added together in order to generate $y_{new}(t)$. The time series at 80m height, $y(t)$ and its phase angles at each frequency till Nyquist frequency are already known. Instead of using these phase angles to generate $y_{new}(t)$, this time, the phase angles are generated randomly by a uniform distribution between 0 and 2π. This random phase generation method is frequently used in Sandia method (8) if information about time series is not available. In this run, only the phaseY is random, other values like auto spectrum P_{yy} and time series for coherence calculation is taken from $y(t)$. The below figures 18 and 19 and table 3 shows the differences in $y(t)$ and $y_{new}(t)$ for the new run.
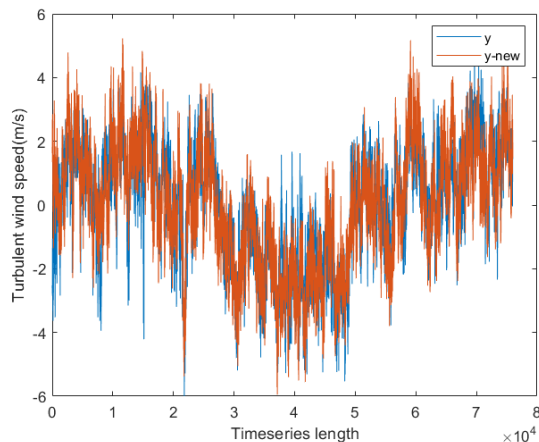
Figure 18: Plot of $y(t)$ and $y_{new}(t)$ with random phaseY

Figure 19: Plot of C_{xy} and $C_{xy}new$ with random phaseY

Table 3: Difference in properties of time series $y(t)$ and $y_{new}(t)$ with random phaseY

	mean	standard deviation
$y(t)$	$3.3e^{-14}$	1.784
$y_{new}(t)$	$-6.3e^{-14}$	1.784

Figure 18 represents the original time series $y(t)$ and the generated time series $y_{new}(t)$ with random phase. The new time series is different but follows the original time series pattern at low frequencies. Overall the values of new time series $y_{new}(t)$ looks different but the standard deviation is identical to the original series. Table 3 shows the average statistical properties of two time series over 10 iterations (because phaseY is generated randomly). From figure 19, the coherence $C_{xy}new$ is higher than the original coherence C_{xy} at high frequencies and this is observed in case1 and very similar to each other at low frequencies and this is observed in case2. Even though this method generates time series very identical to original time series statistically, it still depends on the information from $y(t)$.

3.1.4 Case study 4

In the above method, coherence C_{xy} is calculated from already known time series $x(t)$ and $y(t)$ and used as per Sandia method to generate $y_{new}(t)$. But this time, theoretical coherence function along with random phaseY is used to generate $y_{new}(t)$. The Frost coherence function mentioned in Sandia paper (8) with decay coefficient of 7.5 and mean wind velocity at 40m height are used to calculate theoretical coherence C_{xy}. When fitted the original coherence between $x(t)$ and $y(t)$ with Frost coherence function, the decay coefficient came out to be 10 but this is not used here. The only information taken from $y(t)$ is it's auto spectrum P_{yy}. The below figures 20 and 21 and table 4 shows the differences in $y(t)$ and $y_{new}(t)$ for the new run.
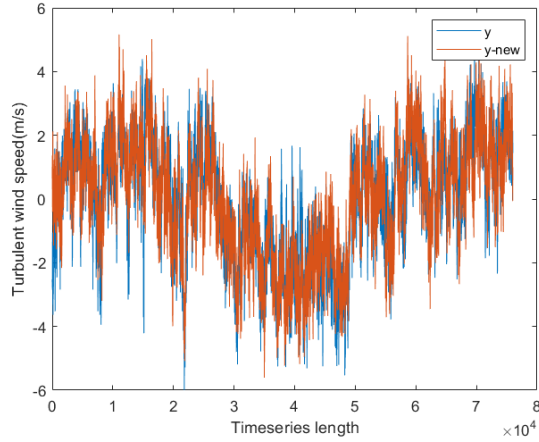
Figure 20: Plot of $y(t)$ and $y_{new}(t)$ with random phaseY and theoretical coherence function
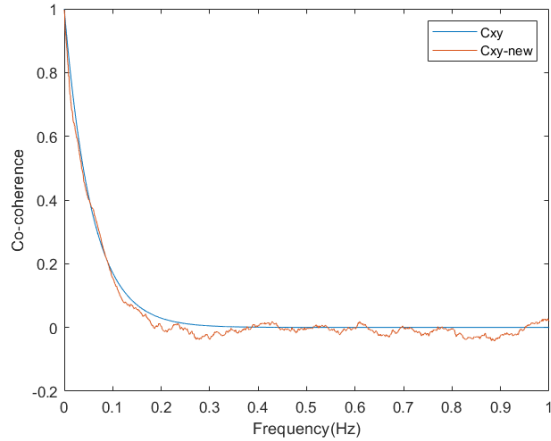
Figure 21: Plot of C_{xy} and $C_{xy}new$ with random phaseY and theoretical coherence function

Table 4: Difference in properties of time series $y(t)$ and $y_{new}(t)$ with random phaseY and theoretical coherence function

	mean	standard deviation
$y(t)$	$3.3e^{-14}$	1.784
$y_{new}(t)$	$-6.5e^{-14}$	1.791

From figure 20, the pattern of generated time series $y_{new}(t)$ is bit different but follows the original time series $y(t)$'s pattern at low frequencies. The turbulent wind speed values of $y_{new}(t)$ are also bit different but the standard deviation is very close to the original series $y(t)$ but not as similar when the coherence C_{xy} is calculated from original time series $x(t)$

29

and $y(t)$ like in case study 3. Table 4 shows the statistical properties of the two time series averaged over 10 iterations (because phaseY is generated randomly). From figure 21, the new coherence $C_{xy}new$ is bit lower than the theoretical coherence C_{xy} at low frequencies but it is very close. $C_{xy}new$ also approaches zero around 0.2 frequency and oscillates around zero. The negative values of the coherence occurs because only the real value of the coherence (co-coherence) is plotted but not the mean squared coherence like in above coherence plots. Co-coherence is plotted here because the theoretical coherence function (ref: Frost function) will approach zero as frequency increases and this can only be achieved by co-coherence but not by mean squared coherence.

The power spectral densities of $y(t)$ and $y_{new}(t)$, P_{yy} and $P_{yy}new$ are plotted over frequency. It can be seen from figure 22 that both spectrum are very close to each other and that the inertial sub range with slope close to $-5/3$ exists. The existence of inertial sub range tells us that the flow is turbulent. It should also be observed that only large eddies that contain most of the turbulent kinetic energy are captured but not small eddies that are responsible for the viscous dissipation of this energy by this measurement frequency of 20Hz.
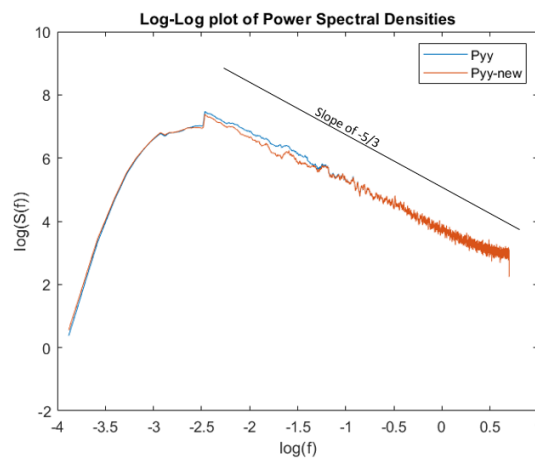
Figure 22: Plot of power spectral densities P_{yy} and $P_{yy}new$

3.1.5 Case study 5

In all the above cases, information from time series $y(t)$ is used either very extensively or nominally in order to generate $y_{new}(t)$. But in reality, information about $y(t)$ might not be available. So, now, only the information from $x(t)$ is used to generate $y_{new}(t)$ and compared with $y(t)$. For this, phaseY is generated randomly from uniform distribution between 0 and 2π, theoretical Frost coherence function with decay coefficient 7.5 is used for C_{xy} and the power spectral density of $x(t)$, P_{xx} is used for P_{yy} ($P_{yy} = P_{xx}$) as input. The below figures 23 and 24 and table 5 shows the differences in $y(t)$ and $y_{new}(t)$ for the new run.

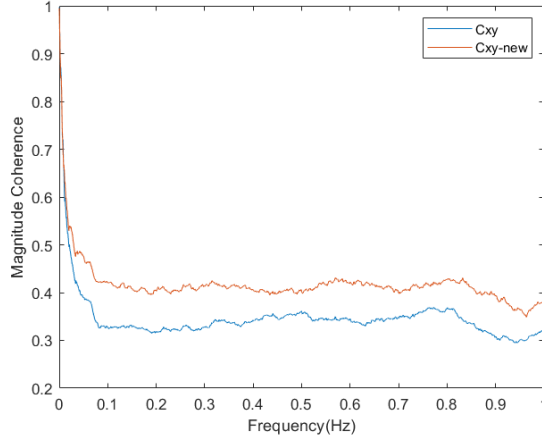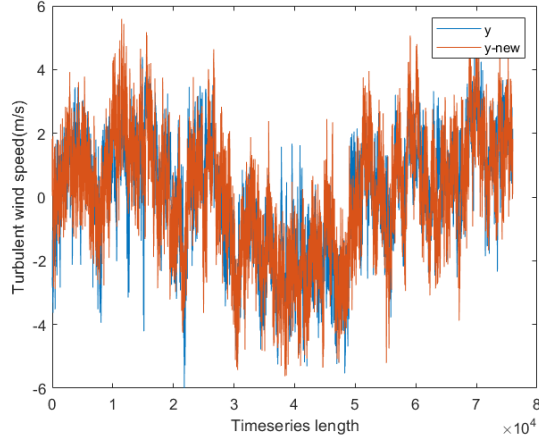Figure 23: Plot of $y(t)$ and $y_{new}(t)$ with random phaseY, theoretical coherence function and $P_{yy}=P_{xx}$
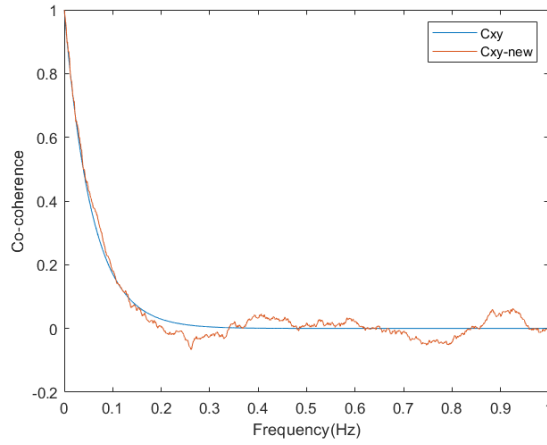
Figure 24: Plot of C_{xy} and $C_{xy}new$ with random phaseY, theoretical coherence function and $P_{yy}=P_{xx}$

Table 5: Difference in properties of time series $y(t)$ and $y_{new}(t)$ with random phaseY, theoretical coherence function and $P_{yy}=P_{xx}$

	mean	standard deviation
$y(t)$	$3.3e^{-14}$	1.784
$y_{new}(t)$	$-10e^{-14}$	1.926

From figure 23, the generated time series $y_{new}(t)$ follows the original time series $y(t)$'s pattern in the low frequency. The values of new time series seems a bit higher than $y(t)$ on

average and this is seen from the standard deviation which increased by 8%. Table 5 shows the statistical properties of the two time series averaged over 10 iterations (because phaseY is generated randomly). From figure 24, the new coherence $C_{xy}new$ is very similar to the theoretical coherence C_{xy} at very low frequencies and a bit higher after but they are very close to each other. Co-coherence is plotted for $C_{xy}new$ and approaches zero around 0.2 frequency similar to C_{xy}

Since only the information of time series $x(t)$ is used as input in Sandia method, the statistical properties of $y_{new}(t)$ are closer to statistical properties to $x(t)$ than $y(t)$ seen from table 6. This means, the auto-spectrum chosen for $y_{new}(t)$ plays a major role in determining it's statistics. Also the pattern of $y_{new}(t)$ is more similar to $x(t)$ than $y(t)$. Figures 25 and 26 shows the plot of $x(t)$ and $y_{new}(t)$ and $x(t)$ and $y(t)$ respectively. It can be seen clearly that the original time series $x(t)$ and $y(t)$ are not so similar as $x(t)$ and $y_{new}(t)$. This is also observed when calculated coherence between $x(t)$ and $y(t)$ is used instead of theoretical coherence function. It seems that coherence has very little influence on the overall statistical properties of the time series as it only exists in low frequencies and the new time series $y_{new}(t)$ follows original time series $x(t)$ over these frequencies. This may also imply that the assumptions made by Sandia method might not be valid for large separation distances.

Note: The turbulent kinetic energy of $x(t)$ is higher than $y(t)$, $P_{xx} > P_{yy}$ because the time series $x(t)$ is measured at 40m height which is most probably inside the surface layer whereas the time series $y(t)$ is measured at 80m height. So, one has to be really careful when applying this method when no information is available.
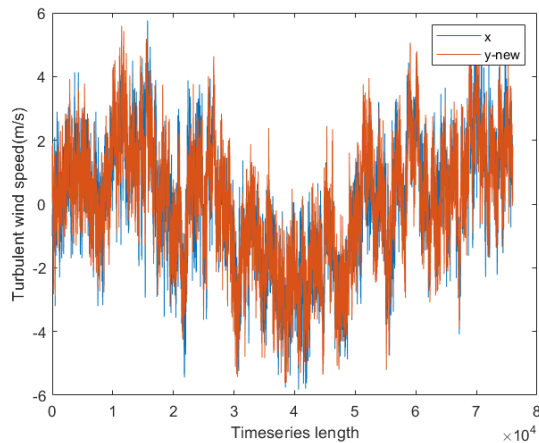
Figure 25: Plot of $x(t)$ and $y_{new}(t)$ with random phaseY, theoretical coherence function and $P_{yy}=P_{xx}$
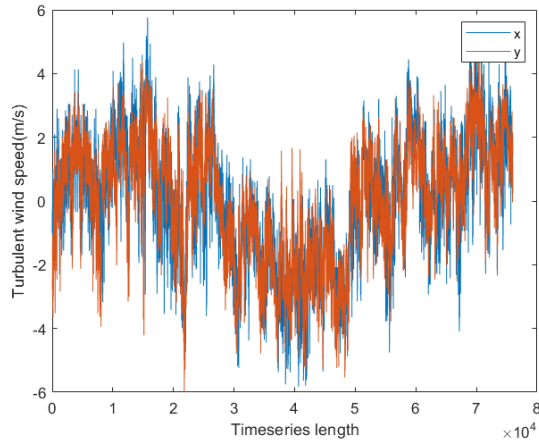
Figure 26: Plot of $x(t)$ and $y(t)$

Table 6: Difference in properties of time series $x(t)$ and $y_{new}(t)$ with random phaseY, theoretical coherence function and $P_{yy}=P_{xx}$

	mean	standard deviation
$x(t)$	$-5.1e^{-14}$	1.906
$y_{new}(t)$	$-10e^{-14}$	1.926

The power spectral densities P_{xx} and $P_{yy}new$ are plotted on a log-log plot. It can be seen from figure 27 that the spectra are similar. This is because $P_{yy}new$ is almost equal to P_{xx}.
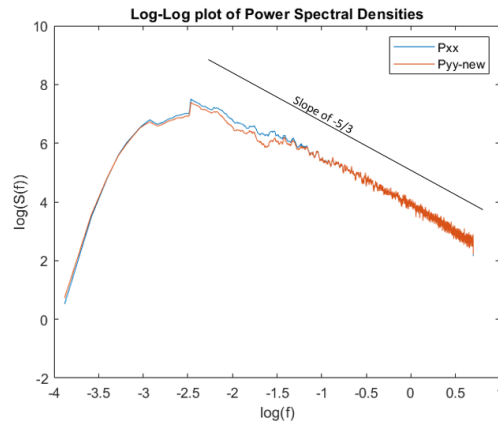
Figure 27: Plot of power spectral densities P_{xx} and $P_{yy}new$

3.2 Summary in generation of $y_{new}(t)$ by Sandia method

A short summary of the the above procedures is listed below. The original time series $x(t)$ and/or $y(t)$ are used to create new time series $x_{new}(t)$ and $y_{new}(t)$ by the use of Sandia method. The Fourier analysis of $x(t)$ and $y(t)$ gives the energy spectrum P_{xx} and P_{yy} and phase values phaseX and phaseY at various frequencies from $[0 \ f_N]$. Only the coherence in along direction (uu-coherence) is considered.

Case 1: Sandia method as mentioned in the paper (8) to generate $y_{new}(t)$
Case 2: Slightly modified method where phaseY is used at H21 instead of phaseX
Case 3: Random phase is used for phaseY with original method
Case 4: Random phase for phaseY and theoretical coherence
Case 5: Random phase for phaseY, theoretical coherence and $P_{yy} = P_{xx}$

Table 7 shows the differences in statistical properties for $y_{new}(t)$ for all the cases.

Table 7: Difference in statistical properties for all cases

	mean	standard deviation
$x(t)$	$-5.1e^{-14}$	1.906
$y(t)$	$3.3e^{-14}$	1.784
Case 1	$-5.9e^{-14}$	2.069
Case 2	$6.6e^{-14}$	2.168
Case 3	$-6.3e^{-14}$	1.784
Case 4	$-6.5e^{-14}$	1.791
Case 5	$-10e^{-14}$	1.926

Even though case 1 supposed to give same results as $y(t)$, it some how gives higher standard deviation indicating an increase in turbulence in the new time series $y_{new}(t)$. This is because of the influence of $x(t)$ in generation of $y_{new}(t)$. Case 2 predicts the coherence between newly generated time series very well but gives even higher standard deviation than case 1. Case 3 seems like an ideal situation where the method re-produces the signal statistically but it depends on the information of $y(t)$ for auto-spectrum, P_{yy} and coherence calculation. Case 4 also gives statistical properties close to $y(t)$ but still depends on spectrum P_{yy}. $y_{new}(t)$ generated by case 5 is completely independent of the information from $y(t)$. Even though the standard deviation increased by 8% compared with $y(t)$, this procedure only depends on one input signal, $x(t)$. Compared with standard deviation of $x(t)$, the standard deviation of case 5 has only increased by 1%. From now on, only the procedure mentioned in case 5 is adapted further assuming one time series is available.

3.3 Rectangular wind field generation

A wind field is required to find loads on a turbine. A code for generation of a wind field based on case 5 of Sandia method has been developed. The wind field developed is for DTU 10MW reference turbine. This turbine has rotor diameter of 178.3m and hub height of 119m. But, for convenience, the diameter has been assumed to be 180m and hub height 120m. Logarithmic wind profile, equation 2 is used to obtain mean wind velocity at hub height with velocity at 10m height $U_{10} = 10m/s$ as reference height and velocity and surface roughness length $Z_0 = 0.01m$ as input. The mean wind velocity at hub height came out to be $U_{hub} = 13.59m/s$.

The wind field generated has the shape of a rectangular box. Since, only the loads on the blades are of interest, the width and height of the rectangular wind field box is same as the rotor diameter, 180m. This width and height is again divided into 20 segments so that wind velocity values are known at every 9m distance as shown in below figure 28.
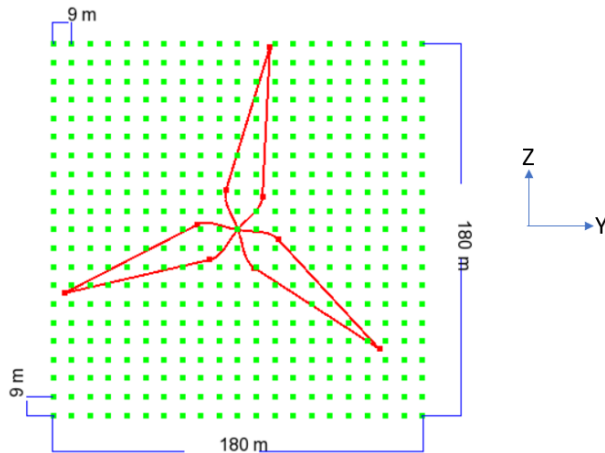
Figure 28: Plot of a frame of known wind speeds at various points on the rotor plane along with the blades of the turbine

In order to generate the wind field box according to Sandia method, information about the spectral matrix (8) is needed as input. This spectral matrix is symmetric where the diagonal contains information about auto-spectra of all the points in the wind field and others cross-spectra which can be found from coherence and auto-spectra. Initially, no information is available about the matrix without wind measurements. One can go with the standards and use theoretical spectrum Kaimal or Von Karman (Kaimal spectrum is commonly used with Sandia method). Instead of directly using a spectral model, time series can also be used to calculate the spectra using Fourier analysis. This code for generation of wind field uses the time series at hub height as input and follows the same procedure as case 5 mentioned above.

The time series at hub height is extracted from a wind field generated in Qblade [2]. This time series is used in the code with the same parameters. The length of the time series is 1024 with time step 0.5 sec. Therefore, the total time is 512 sec. By the assumption of Taylor's hypothesis, (1) time scale can be converted into length scale with the help of mean wind velocity at hub U_{hub}. The length scale is $U_{hub} * 512$ which is approx. 6958m. Therefore, the rectangular wind field box has dimensions LxBxH as 6958x180x180. This wind field box is projected on to the rotor plane of the turbine with velocity U_{hub} in order to find time series of structural loads. An animated movie of the wind field has been made for visualization.
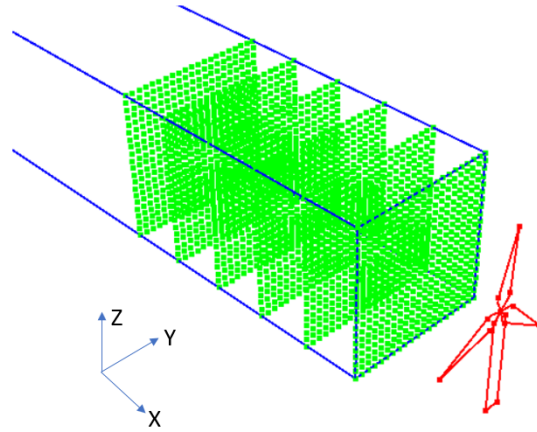
Figure 29: Plot of a rectangular box wind field projecting on a turbine

The input parameters used for generation of wind field are:

- Length of time series, 1024 steps

- Timestep, 0.5 sec

- No. of points in across wind direction (along Y axis), 21

- No. of points in vertical wind direction (along Z axis), 21

- Distance between each point along Y axis, 9m

- Distance between each point along Z axis, 9m

- Mean wind velocity at hub height, 13.59 m/s

- Mean wind velocity at 10m height, 10 m/s

- Surface roughness length, 0.01m

[2]Qblade is an open source software on design of wind turbines developed at TU Berlin

- Tubulent Intensity, 10%

- Hub height, 120m

- rotor radius, 90m
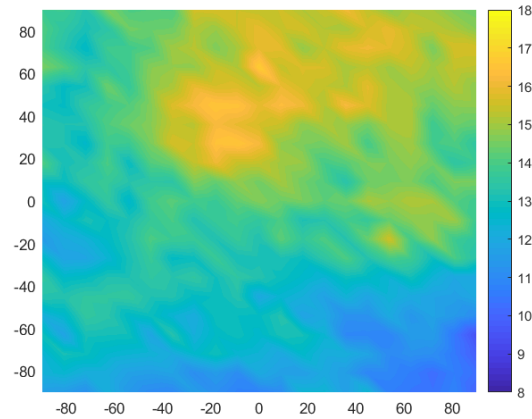
Figure 30: Plot of snapshot from animated wind field. The color bar on the right side suggests wind speed in m/s

3.3.1 Comparison with wind field from Qblade

The wind field that has been generated above (called as Sandia in this section) is compared statistically with the wind field from Qblade where time series at hub is taken from for one realization. Figure 31 shows the standard deviation plotted for all the points (441) in wind field from left to right and bottom to top.
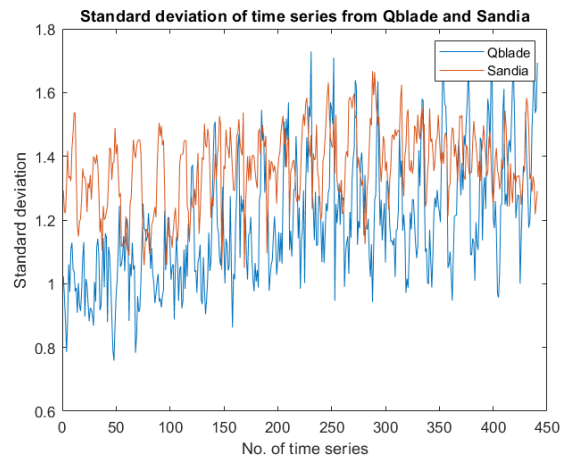
Figure 31: Plot of standard deviation of time series of wind fields from Qblade and Sandia

The standard deviation from Qblade increases with height in the wind field. This is because, as the mean wind velocity increases with height, the standard deviation must increase in order to keep the turbulent intensity (T.I) constant as $T.I = std/mean$. This behaviour is opposite in real atmosphere where the standard deviation of wind velocities decreases with height (16).

The standard deviation of the wind field from Sandia is more or less constant[3]. If the mean wind speed increases with height and the standard deviation is constant, then the T.I decreases with height. This is observed in real atmosphere where the turbulent kinetic energy decreases with increasing height in neutral atmosphere. Even though this phenomenon is not included in the procedure, it justifies the decrease in turbulence with height.

Figure 32 shows the coherence between hub center and points along the upper Z-axis with an interval of 9m distance in the wind fields. The theoretical Frost coherence functions for various separation distances can be seen in figure 34b. The wind field from Sandia method shows better coherence than the wind field form Qblade. For large separation distances, Qblade cannot capture the coherence at low frequencies. Also, the coherence dies out rapidly even for small separations.
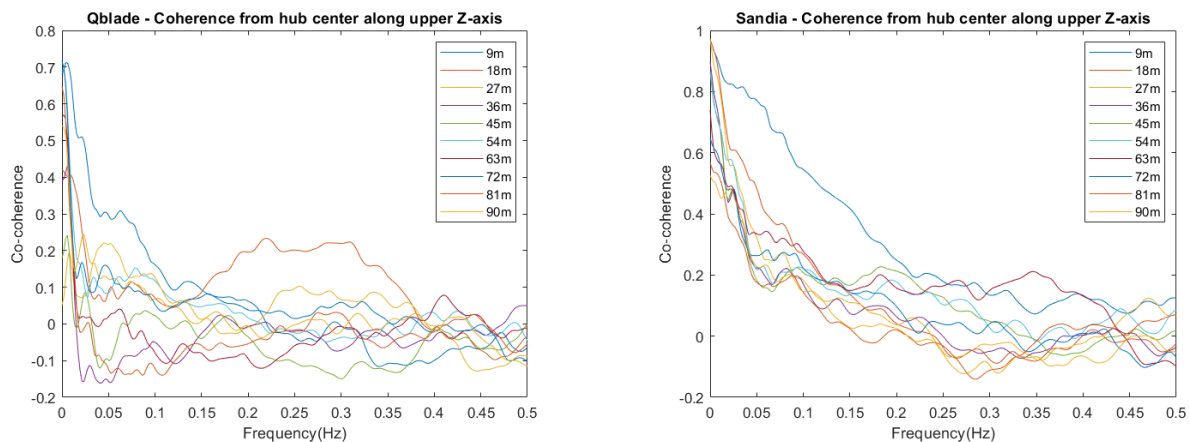
Figure 32: Plot of Co-coherence between hub center and points along upper Z-axis in the wind fields from Qblade and Sandia

Figure 33 shows the coherence for near and far separation distances from hub center for both wind fields along with Frost theoretical coherence function. It can be seen that Sandia wind field represents the theoretical coherence better than Qblade even though it predicts a bit higher coherence at low frequencies.

---

[3]The standard deviation of the input signal is 1.29 where as the average standard deviation of the wind field is 1.36. There is an 5% increment
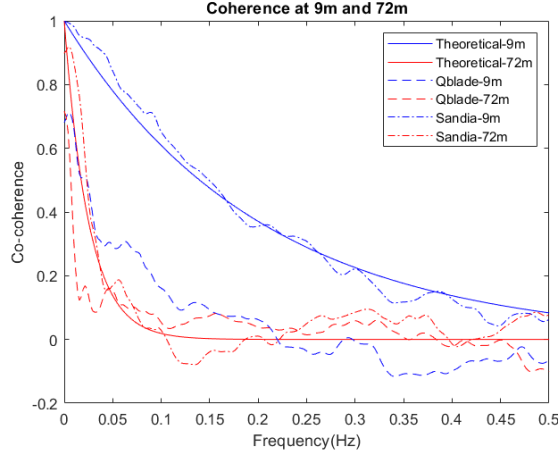
Figure 33: Plot of co-coherence between hub center and 9m and 72m along upper Z-axis for Qblade and Sandia wind fields

3.3.2 Modified wind generation method

The method adapted above generates time series at each point in the wind field sequentially. Even though the time series are generated sequentially, it does not include the phase information of already generated time series to generate next one. So, a slightly modified version of the wind generation method has been investigated where the phase information of already generated time series has been used to create the next time series. More clear explanation follows with an example.

Let's say we have an initial time series $x(t)$ at the hub center. We want to generate 2 new time series $y(t)$ and $z(t)$ at 9m and 18m distance from the hub. First, the time series $y(t)$ is generated according to the procedure mentioned in case 5 from theoretical coherence C_{xy}, P_{xx}, phaseX and phaseY. phaseY used here is generated randomly by an uniform distribution in the range $[0\ 2\pi]$. But, once the time series $y(t)$ is known, Fourier analysis of $y(t)$ gives new spectrum and new phase information, say P_{yy} and phaseY2. P_{yy} will be close to P_{xx} and phaseY2 will be close to phaseY only at high frequencies but not at low frequencies because of the influence of phaseX in generation of time series $y(t)$. The time series at 18m, $z(t)$ can be generated either by using random phase (phaseY) or Fourier analysis phase (phaseY2). The original method still uses phaseY. A slightly modified method is proposed where phaseY2 is used i.e, the original random phases chosen for $y(t)$ corrected for the correlation with $x(t)$.

Using time series at hub center as input, new time series of wind velocities are developed based on original and modified method along upper Z-axis (assuming the origin is at hub center) at every 9m interval until 90m (rotor radius). In total, there are 10 different time series generated for each method. Coherence between hub center time series and the generated time series are calculated to compare with the input theoretical coherence functions in order to validate the authenticity of each method.

39
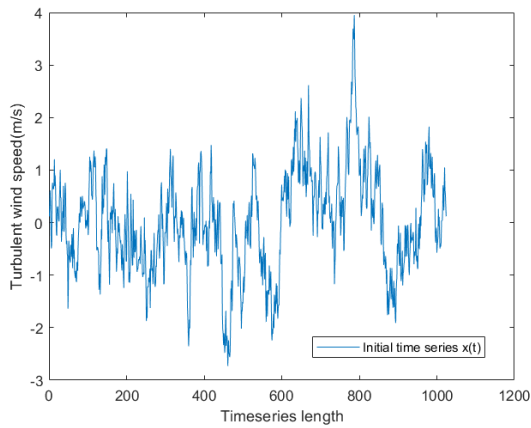
(a) Plot of initial time series at hub center
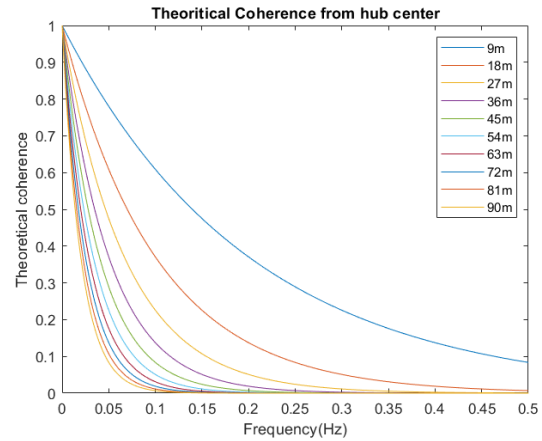
(b) Plot of theoretical coherence

Figure 34: Plot of time series at hub height and theoretical coherence functions at various separation distances

Figure 34a shows the time series at hub center and figure 34b shows the theoretical coherence between hub center and at a distance along the rotor radius, which are used as input for original and modified method.
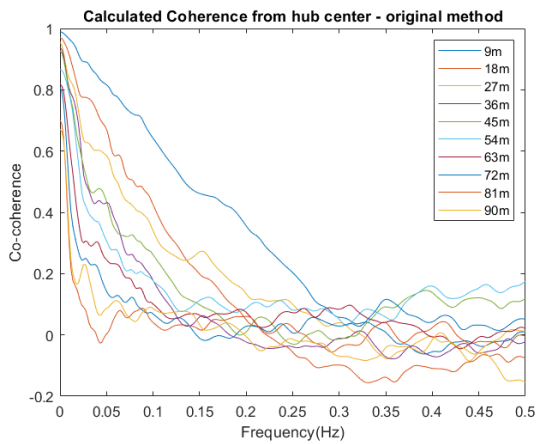
(a) Plot of calculated co-coherence for original method
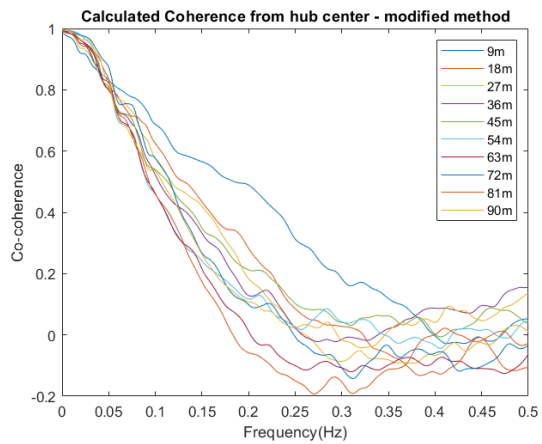
(b) Plot of calculated co-coherence for modified method

Figure 35: Plot of co-coherence at various separation distances from hub center for original and modified method

Figures 35a and 35b shows the coherence calculated from the time series generated based on original and modified method respectively for a random realization. It can be seen that the coherence of the original method is close to the theoretical coherence (figure 34b) than modified method. Modified method shows high coherence even at larger separation distances. However it reaches unity when frequency approaches zero and the curvature changes to convex upwards. Original method does not reach unity when frequency approaches zero for large separations. This phenomenon is observed in real flow measurements (10) and (17). The frost coherence function approaches unity even for larger separation distances when frequency approaches to zero but original method doesn't.

Figures 36a and 36b shows the plots of the generated time series for original and modified method including input time series. The time series generated by original method follows the pattern of the input time series a bit while the time series generated by modified method follows very close. When the no. of points in the wind field (no. of time series to be generated) increases, it becomes even tougher for the time series generated by original method to follow the pattern of the input time series as the randomness in the model increases. While on the other hand, the total energy of the time series generated according to modified method has increased drastically compared with the total energy of the input time series. This keeps on increasing with increasing no. of points in the wind field. From figure 34a, the input time series of turbulent wind speeds at hub center has range [-3 4]m/s while figure 36b shows that the time series generated by modified method has range [-8 10]m/s. This gives much higher energy than the input energy. When the whole wind field (rectang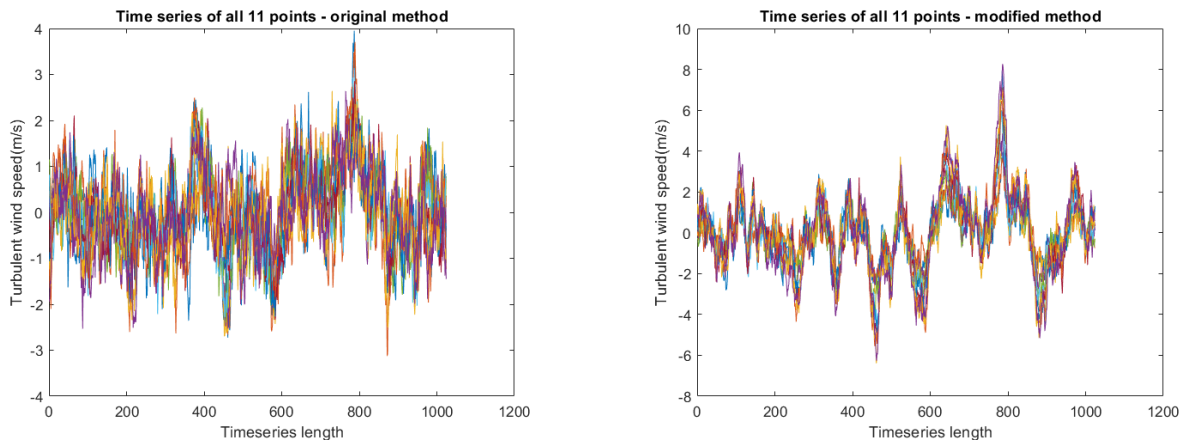ular box) has been generated according to modified method, turbulent wind speeds as high as 20m/s are observed. Obviously this is wrong. Where as, from figure 36a, the time series generated by original method has range from [-4 4]m/s which is close to the range of input time series. This range and total energy hasn't change much even when the whole wind field is developed.

(a) Plot of time series generated by Sandia method

(b) Plot of time series generated by modified Sandia method

Figure 36: Plot of 11 time series along upper Z-axis for original and modified method

In short summary, two different rectangular wind fields are developed based on the procedure of case 5 as mentioned in section 3.1.5. One where only random phases are used and other, the random phases are corrected for the correlation with input time series. This correction increases the turbulent kinetic energy drastically and gives high coherence even at large separations. So, only the wind field generated by random phases is considered further.

3.4 Polar wind field generation

The wind field generated by Sandia method is a rectangular box with information about wind velocities at various points in space. This box is projected onto the DTU 10MW Horizontal Axis Wind Turbine(HAWT). The box has width and height as the rotor diameter of HAWT. Since, the blades of the turbine rotates in a circular motion, and the wind field is rectangular, it is possible that the wind speeds at a particular location on the blade is not available for a particular time step and have to interpolate from the nearest points on to the blade. The interpolation procedures can be debatable since turbulent wind speeds are stochastic.

In order to avoid interpolations and find wind speeds at exact locations on the wind turbine blades at every instant, a circular wind field using cylindrical co-ordinates is developed with the same parameters as the rectangular wind field. This wind field looks like a cylinder with length equal to the length of the rectangular wind field box and has a diameter equal to the rotor diameter. The DTU 10MW wind turbine rotates with approx. 10 rpm. This is equal to $\frac{\pi}{3}$ rad/s. The time step of the input time series is 0.5 sec. This means, the blade rotates $\frac{\pi}{3} * 0.5 = \frac{\pi}{6}$ degrees every single time step. Therefore, 12 points are needed on each circle in order to have sufficient frequency resolution since $\frac{\pi}{6} * 12 = 2\pi$.

The HAWT rotor has a radius of 90m which is divided into 10 segments with each segment of length 9m. The polar wind field is generated in a way that wind speeds are known at every 9m on the blade as shown in figure 37.
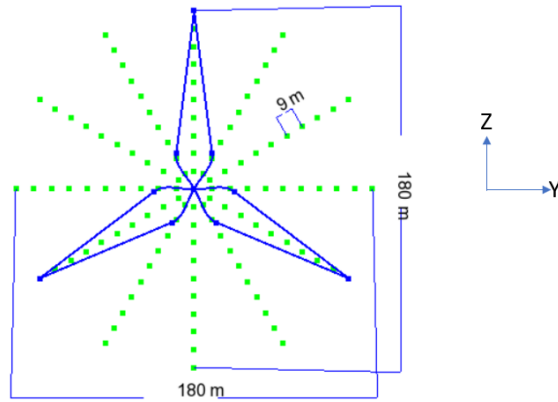
Figure 37: Plot of a frame of known wind speeds at various points radially on the rotor plane along with the blades of the turbine

Figure 37 shows that radially distributed points coincides exactly with the blades which wasn't the case with the rectangular wind field, figure 28. Also, the no. of points in each frame reduced from 441 to 121 which makes the simulation time much less for a polar wind field.
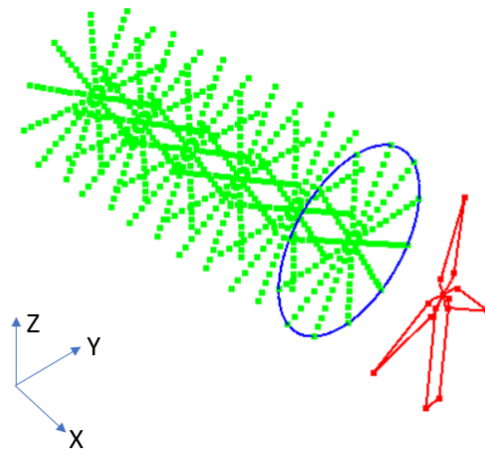
Figure 38: Plot of a polar wind field along with HAWT

The polar wind field has a total of 121 different time series including input time series at hub center. The standard deviation of input time series is 0.98. The average standard deviation of all 120 generated time series is 1.04. There is a 6% increase in the value but this is expected based on the procedure (case 5).

43

3.4.1 Coherence plotting methods

The coherence in along wind direction between hub center time series and 120 generated time series are calculated for a realization of a polar wind field. There are 12 points at equal separation distance from hub center at every 9m interval. Average is taken for these 12 points and only one coherence plot is plotted for each separation distance. So, in total, there will be 10 coherence plots. Figure 39 shows these 10 coherence plots along with input theoretical coherence function.
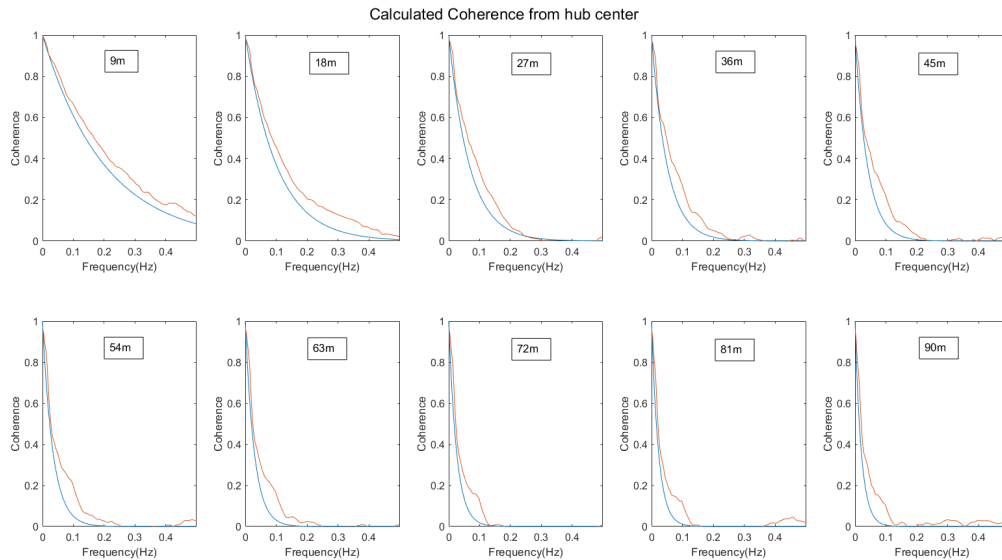
Figure 39: Plot of averaged coherence from hub center to all distances. Red - calculated average co-coherence, Blue - theoretical coherence

Instead of averaging the coherence of 12 points at every separation distance, another way of plotting coherence is looked at. Concatenation of time series. All the 12 time series at a certain separation distance are concatenated and coherence is plotted between hub center time series and the concatenated time series.
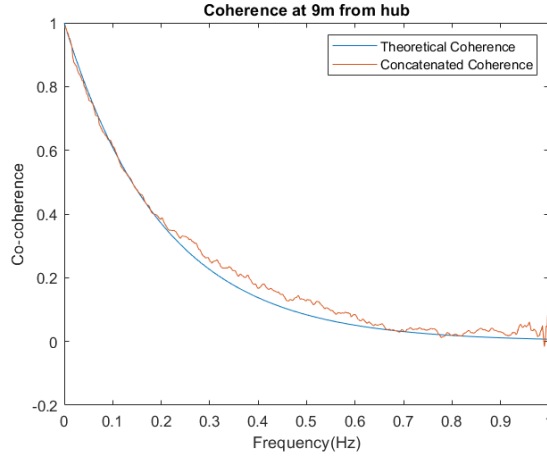
Figure 40: Plot of concatenated co-coherence between hub center and 9m separation points along with theoretical coherence
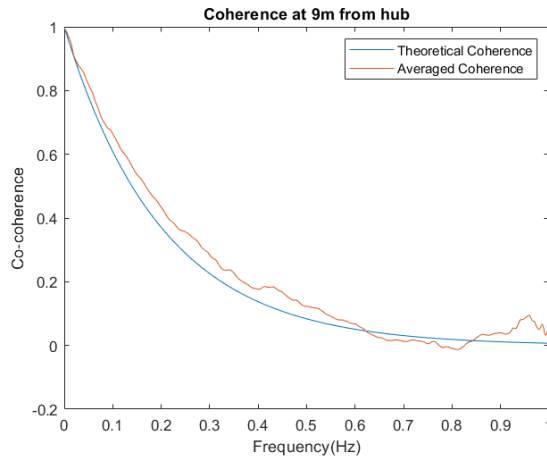
Figure 41: Plot of averaged co-coherence between hub center and 9m separation points along with theoretical coherence

Figure 40 shows the coherence plot between hub center and concatenated time series at 9m separation and figure 41, the averaged coherence. It can be seen that the concatenated coherence represents the original coherence function better than the averaged coherence and especially at low frequencies where coherence is higher. The reason could be reduction in margin or error (18). Margin of error(MOE) for a sample is given as:

$$MOE = Z * \frac{\sigma}{\sqrt{N}} \tag{14}$$

where,

Z = Z-score value for a certain confidence interval
σ = standard deviation of the sample
N = sample size

When coherence is calculated by concatenation procedure, the length of the time series becomes 12*1024 = 12288 and window size is taken to be 1024 which is the size of each individual time series. So, the sample size for this procedure is 1024. Averaged coherence is made with average of 12 coherence functions that are calculated with 12 time series each of length 1024 and window size of 128. The sample size for this method is 128.

As MOE is inversely proportional to the square root of sample size, MOE decreases with increasing sample size. So, the averaged method will have high error than concatenated method. This high error that exists initially for all 12 coherence functions will be averaged but not reduced.

3.5   Bending moment calculations on a beam

Once a polar wind field is generated with sufficient spatial and temporal resolution, structural loads on the turbine blades can be calculated using the wind velocities from the wind field. The wind velocities are known at every 9m on the blade with a frequency of 2Hz. The global structural response - root bending moment of the blade is investigated for various cases depending on the variation in wind shear and/or turbulence in the wind field. The polar wind field that is considered for calculating bending moments have U_{hub} as 17.7m/s, roughness length 0.01m and turbulent intensity 10%.

3.5.1   Fixed cantilever beam

But first, an ordinary cantilever beam (fixed at one end) of the same length as the blade is taken to see how the forces look like in general. The beam is placed in the wind field and checked for root bending moment (bending moment at the fixed end). No structural deformations are taken into account assuming that the beam is stiff and also mass free. The beam is assumed to have a circular cross section with 4m diameter and drag coefficient (C_d) as 0.5. C_d depends on the Reynolds number. Since, atmospheric turbulent flows have high Reynolds number, the choice for the value of C_d can be justified (19).

The beam is placed along the Z-axis on the lower half of the polar wind field as seen in figure 42. The beam is also divided into 10 segments each of 9m length and drag forces are calculated at the mid-point of each segment. Using these drag forces and the distance from the fixed end, bending moment at this end can be calculated. Bending moment for various cases of the wind loads have been investigated.

Load case 1: Homogeneous wind field i.e, without wind shear and turbulence. The wind velocities in the whole wind field are considered to have U_{hub}

Load case 2: Steady wind field i.e, with wind shear but without turbulence

Load case 3: Ordinary wind field i.e, with wind shear and turbulence

Table 8 shows the mean and maximum bending moment for different load cases. The homogeneous and steady wind field have same mean and maximum because the wind velocities are not changing over time. However, load case 1 have higher bending moment and this is because, for load case 2, the wind velocities decrease from fixed to free end due to shear. Comparing load cases 2 and 3, including turbulence has almost no effect on the mean but significantly increases the maximum bending moment.
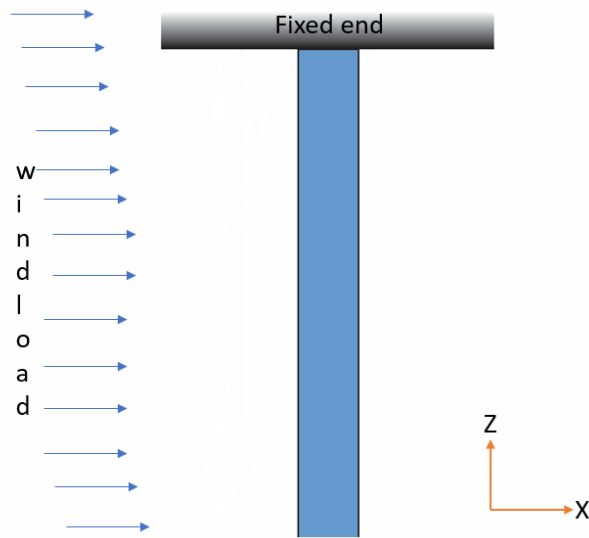
Figure 42: Plot of the cantilever beam placed in the wind field (6)

Table 8: Bending moment values for various load cases on a fixed cantilever beam in N-m

Load case	Mean	Maximum
1	$1.2665e^6$	$1.2665e^6$
2	$1.0718e^6$	$1.0718e^6$
3	$1.0793e^6$	$1.5853e^6$

Figure 43 shows the drag forces on all segments of the beam for the 3 load cases for a random time step of wind loads. The drag force doesn't change along the beam for load case 1, decreases for load case 2 and random for load case 3. Bending moment values for all time steps for the load cases can be seen in figure 44. The bending moment values doesn't change for load cases 1 and 2 and random for load case 3.
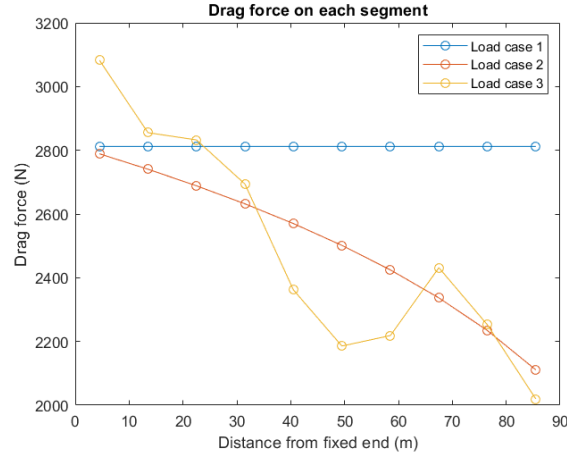
Figure 43: Plot of drag force on each beam segment for the 3 load cases for a random time step
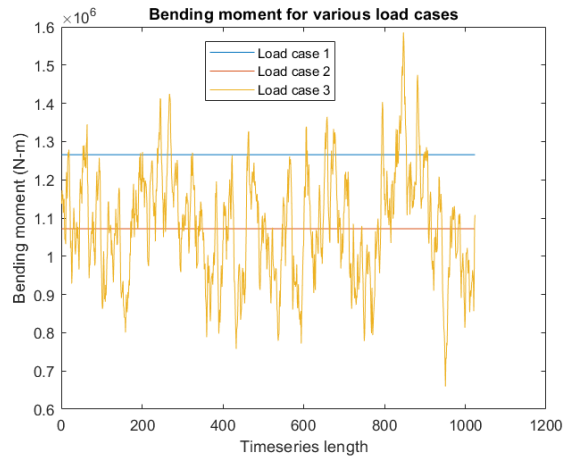
Figure 44: Plot of bending moment at the fixed end for the 3 load cases for all time steps

3.5.2   Rotating cantilever beam

The same beam is made to rotate like HAWT. Now, it will have X-rotational degree of freedom free instead of fixed. The rotational velocity is taken to be 10 rpm which is the same as the DTU 10MW blade's rotational velocity at/above rated wind speed. Only load case 3 with wind shear and turbulence in the wind field along with the rotation is presented. Let's call this load case 4 (load case 3 + rotation). Other load cases 1 and 2 with rotation can be seen in appendix B.

Table 9: Bending moment values for load cases 3 and 4 in N-m

Load case	Mean	Maximum
3	$1.0793e^6$	$1.5853e^6$
4	$1.9150e^7$	$1.9855e^7$

Table 9 shows that the bending moment values for load case 4 increased more than 10 times compared with load case 3. This means, the bending moment due to rotational velocities dominates over the bending moment due to actual wind velocities at above rated wind speed. This is because the rotational velocities increase linearly with radial distance. For a beam rotating with 10rpm and radius 90m, tip rotational speed will be over 90m/s while wind velocities will only be around 17.7m/s. The total velocity is calculated as shown in below figure 45.
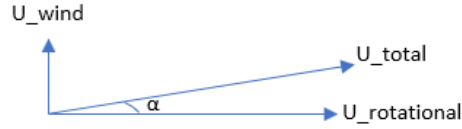
Figure 45: Plot of total velocity calculation

Using U_{total}, drag forces can be calculated which in turn used to calculate bending moment. It should be noted that due to turbulence U_{wind} changes every time step and so does α. This means, the direction of drag force changes a bit every time step due to turbulent wind speeds but this is neglected.

Figure 46 shows the plot of root bending moment for load case 4. This bending moment does not have high standard deviation because bending moment due to rotation which has higher influence is constant for all time steps.
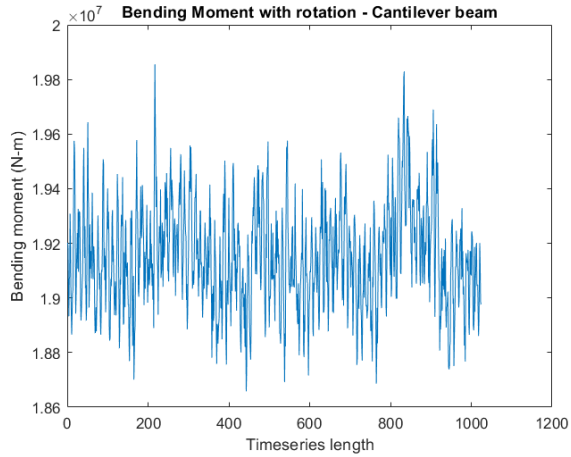
Figure 46: Plot of bending moment of a beam with rotation placed in the polar wind field

Figure 47 shows the plot of drag force on the beam for a random time step. It can be seen that the drag force increases with the power 2 radially along the beam.
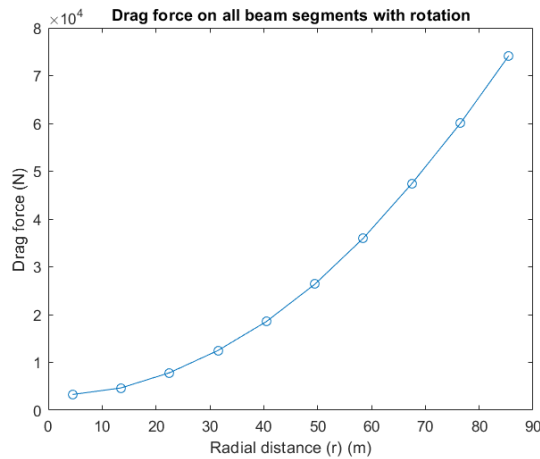
Figure 47: Plot of drag forces on the beam with rotation for a random time step

Drag forces without mean have been plotted for segments closest and farthest from the hub to check for drag force variability. Figure 48 shows the drag force values without mean for all time steps for segment 1 and 10. Segment 1 being close to the hub and segment 10 the farthest. Clearly forces at segment 10 have higher variability due to larger variations in the wind velocities because of shear. It should also be observed that segment 10 follows the pattern of segment 1 indicating the coherence in the wind field.
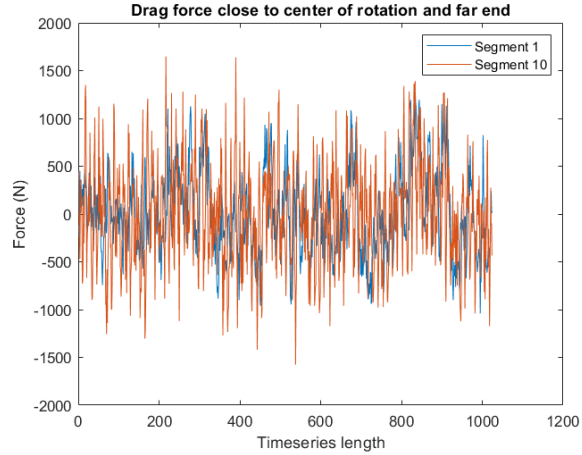
Figure 48: Plot of drag force variability at segment 1 and segment 10 of the beam with rotation

3.6 Bending moment calculations on a blade

Now, the polar wind field is projected on to an actual DTU 10MW HAWT with rated rotor speed of 10 rpm. The turbine blades will have airfoil cross sections where both lift and drag forces exist. The blade has different airfoil types over the span. Information about blades and airfoils can be found in (7). The blade is divided into 10 segments of 9m length in order to apply 2D Beam Element Momentum (BEM) theory. For each 9m span of the blade, chord length is averaged and assumed an airfoil type (common for that span) of this chord length. Using these chord lengths and distances from hub center, twist angles of the blade are extracted. The pitch of the blade with 17.7m/s mean wind speed at the hub and axial induction factor[4] of 0.2 is 9.87deg. Pitch + twist gives θ (figure 5). Table 10 shows the twist angle and airfoil type for each segment of the blade.

---

[4]The choice of axial induction factor value comes from BEM theory

Table 10: Twist angle, θ and airfoil type for each segment of the blade (7)

Segment length (m)	Mid-point distance (m)	Chord length-average (m)	Twist (deg)	θ (deg)	Airfoil section type
0 - 9	4.5	5.38	14.5	24.4	CYLINDER
9 - 18	13.5	5.65	13.9	23.8	FFA-W3-600
18 - 27	22.5	6.15	9.0	18.9	FFA-W3-480
27 - 36	31.5	6.00	6.4	16.3	FFA-W3-360
36 - 45	40.5	5.42	4.8	14.7	FFA-W3-300
45 - 54	49.5	4.70	3.0	12.9	FFA-W3-300
54 - 63	58.5	3.90	1.2	11.1	FFA-W3-240
63 - 72	67.5	3.15	-0.5	9.4	FFA-W3-240
72 - 81	76.5	2.49	-1.8	8.1	FFA-W3-240
81 - 90	85.5	1.58	-3.0	6.9	FFA-W3-240

From 2D BEM theory, an axial induction factor of 0.2 gives the required power output. The average power from calculations came out to be 11MW. Considering 10% losses from gears and generator, required power output of 10MW at above rated wind speed is achieved. However, the thrust forces from calculations and Betz theory are different. If the axial induction factor is adjusted to achieve same thrust forces, power output has decreased. This theory is very sensitive to the choice of axial induction factor. Since, power output of 10MW has to be achieved at above rated wind speed, axial induction factor is kept at 0.2 for further analysis. The thrust forces are not balanced because the BEM theory applied here is a simplified version. Corrections like tip losses, Glautert limit, 3D effects have not been considered. But, this should be okay since we are only looking for the relative importance of various load cases.

By 2D Blade Element Momentum (BEM) theory, the angle of attack, α can be calculated ($\alpha = \phi - \theta$, figure 5) for every time step and for every segment of the blade. Using α, stationary lift and drag coefficients (C_L, C_D) can be extracted and used to find lift and drag forces.Using lift, drag and ϕ, thrust on the blade perpendicular to the rotor plane at each segment is calculated. Using thrust and segment distance from hub center, flap-wise bending moment is calculated.

The force that is parallel to the rotor plane which drives the rotation of the blade is also calculated from lift,drag and ϕ. Using this force and segment length, bending moment due to rotation is calculated. The mass of each blade is 41716kg with center of gravity at 21.2m span from hub center. Using this, bending moment due to gravity is also calculated. The sum of bending moment due to gravity and rotation gives edge-wise bending moment.

3.6.1 Blade load cases

Like in the case of cantilever beam, different load cases have also been investigated on the blade based on wind shear and turbulence in the wind field which are listed below. Neutral atmospheric conditions are assumed. Wind shear is calculated based on logarithmic wind profile and turbulent intensity is 10%. When no shear in the wind is assumed, the mean wind velocity at the hub ($U_{hub} = 17.7m/s$) is considered as the mean wind velocity for the whole rotor plane. Table 11 shows the mean and maximum bending moments for flap-wise and edge-wise. The maximum cycle height for edge-wise is the difference between maximum and minimum value for all time steps of the wind field. The values given are for one realization of a wind field and the same turbulent time history is used for all the load cases.

Blade load case 1: No shear and no turbulence
Blade load case 2: With shear and no turbulence
Blade load case 3: No shear and with turbulence
Blade load case 4: With shear and turbulence (ordinary scenario)

Table 11: Bending moments for various cases of the blade in N-m

Blade load case	Mean flap-wise bending moment	Maximum flap-wise bending moment	Mean edge-wise bending moment	Maximum edge-wise bending moment	Maximum cycle height edge-wise
1	$1.6027e^7$	$1.6027e^7$	$3.5485e^6$	$1.2187e^7$	$1.7316e^7$
2	$1.5696e^7$	$1.7678e^7$	$3.4698e^6$	$1.2187e^7$	$1.7316e^7$
3	$1.6025e^7$	$2.5811e^7$	$3.6035e^6$	$1.5931e^7$	$2.2570e^7$
4	$1.5694e^7$	$2.5811e^7$	$3.5249e^6$	$1.5931e^7$	$2.2570e^7$

Table 12: Standard deviation of bending moments in N-m

Blade load case	Standard deviation flap-wise bending moment	Standard deviation edge-wise bending moment
1	0	$6.1252e^6$
2	$1.6333e^6$	$6.1456e^6$
3	$2.4564e^6$	$6.1618e^6$
4	$2.9499e^6$	$6.1818e^6$

From table 11, the mean flap-wise bending moment increases by a small amount around 2% when wind shear is absent. This can be explained by a small example. Let's take segment 10 (at tip) of the blade for analysis. The mean wind velocity at segment 10 without shear is U_{hub}, 17.7m/s. The mean wind velocity at segment 10 with shear when it is at the top of

the wind field is 18.7m/s and at bottom of the wind field is 15m/s. The average mean wind velocity in shear is 16.85m/s. For large rotational velocities, the wind velocity is proportional to the flow angle (ref: equation 11). The angle of attack increases with increasing flow angle. And, the forces on the blade are proportional to the angle of attack (ref: equations 12 and 13). So, the forces are proportional to wind velocity. Due to this, there is a slight reduction in mean forces when shear is present. Also, the slope of the wind profile keeps on changing with height when shear exists. Figure 49 shows that the increment of wind speed from hub center and above is lesser than the decrement from hub center and below from U_{hub}. On the other hand, turbulence has almost no influence on mean flap-wise bending moment because the mean turbulent velocity is zero.
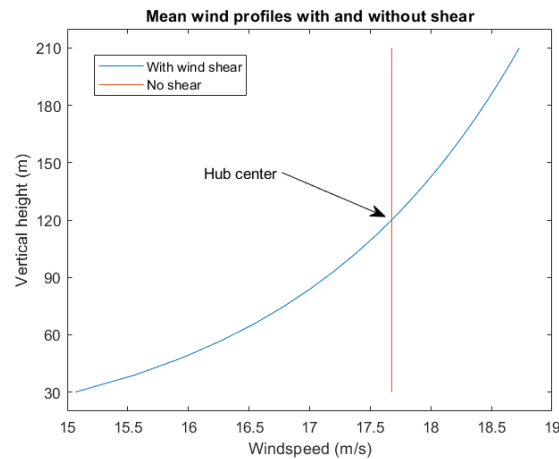

Figure 49: Plot of wind profiles for the rotor diameter with and without shear

Shear has some influence on maximum flap-wise bending moment. Comparing case1 and case2 when there is no turbulence, the value increases by 10%. And, comparing case3 and case4 when turbulence exists, wind shear has no influence on maximum flap-wise. This is because the maximum occurs at a time step when the blade is horizontal (along Y-axis) in the wind field. Then the loads on the blade will be the same for both cases. Otherwise, a slight increase in maximum values should be expected due to wind shear. Anyways, Shear has more influence on maximum flap-wise bending moment when turbulence is not present which is highly rare in real atmosphere.

Turbulence increases maximum flap-wise bending moment. Comparing case2 and case4, when wind shear is present, turbulence increases the maximum value by 46%. And, comparing case1 and case3 with no shear, the value increases by 61%. Even though these values are for a single realization, turbulence has more influence when wind shear is absent which is also highly unlikely in reality because of the presence of the ground. In general, turbulence has a lot of influence on maximum flap-wise bending moment.

Similar behaviour is also observed in edge-wise bending moment. Lack of shear increases the mean edge-wise bending moment a bit and turbulence has almost no effect on the mean. The maximum edge-wise bending moment is not influenced by wind shear at all. This is because, the bending moment due to rotation which is influenced by shear is smaller than gravitational bending moment which is not influenced by shear. The maximum gravitational bending moment occurs when the blade is horizontal in the wind field. When the blade is horizontal, the mean wind speeds along span of the blade are equal (to U_{hub}) with or without shear. On the contrary, introducing turbulence increases the maximum edge-wise bending moment and cycle height by around 30%.

From table 12, the standard deviation (std) of flap-wise bending moment when no shear and turbulence is present is zero because of constant bending moment value for every time step. Introducing shear increases the std (case2) but introducing turbulence increases the std even higher (case3). Case4 has the highest std because of high variability in the wind due to shear and turbulence. While for edge-wise bending moment, not a lot of variation in std has been observed because most of the bending moment is due to gravity. The slight variation that has been observed follows the same pattern as flap-wise bending moment.

So, overall, wind shear has more influence on mean bending moment and turbulence on max bending moment. The magnitude of influence of shear on mean is small compared to turbulence on maximum but not negligible. Both shear and turbulence has an effect on standard deviation but the effect of turbulence is higher.

3.6.2 Blade load case 4

The results from blade load case 4 where both wind shear and turbulence exists in the wind field are presented below. Other load cases results can be seen in appendix C.
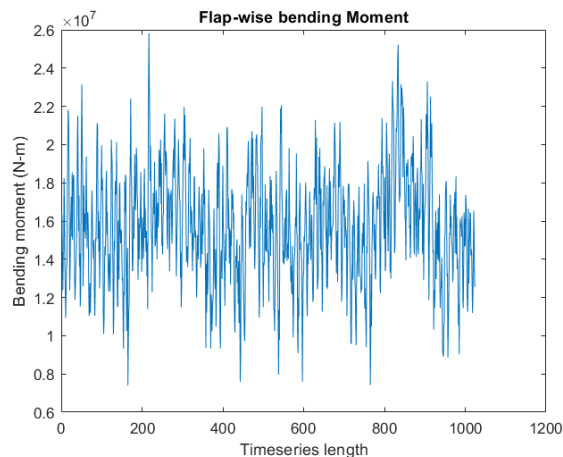

Figure 50: Plot of flap-wise bending moment for blade load case 4

Figure 50 shows the bending moment at the root of the blade due to the forces normal to the rotor plane which is called flap-wise bending moment. The mean flap-wise bending moment is $1.5694e^7$ N-m and standard deviation is $2.95e^6$ N-m. The standard deviation is small compared to the mean. This implies that the mean value does not vary much except when high turbulent speeds are encountered. This is again because most of the bending moment comes due to rotational velocities which are high compared to wind velocities and does not change at above rated wind speed. The maximum bending moment for all the time steps is $2.5811e^7$ N-m. The blade has to be designed to have a structural strength to withstand this maximum bending moment.

Figure 51 shows the input turbulent velocity time series at hub used to create the polar wind field which in turn used to calculate the flap-wise bending moment by BEM theory. It can be seen from figures 50 and 51 that some coherence exists between these two at very low frequencies. But, the maximum bending moment does not occur when the turbulent velocity at hub is maximum because of the influence of shear and other turbulent velocities along the blade. Since, turbulence has a lot of influence on the maximum bending moment values, it should be highly necessary to get the wind field as accurate as possible.
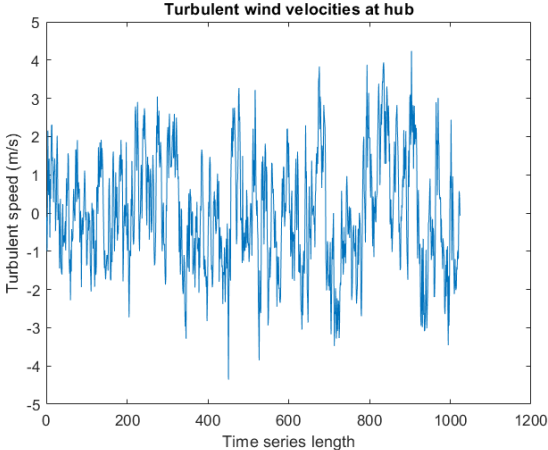

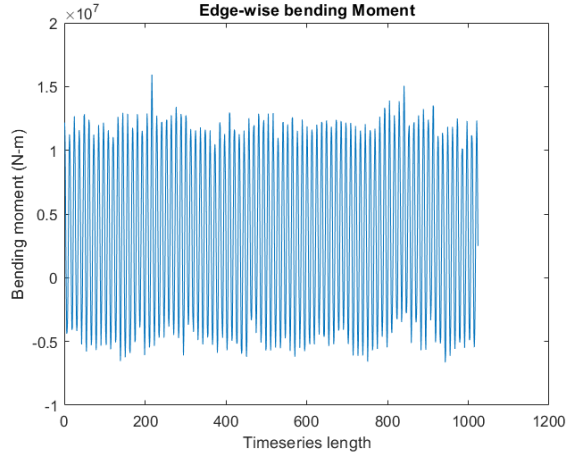Figure 51: Plot of input time series of turbulent wind velocities at hub for the polar wind field

Figure 52: Plot of edge-wise bending moment for load case 4

Figure 52 shows the bending moment at the root of the blade due to the forces parallel to the rotor plane which is called edge-wise bending moment. The mean edge-wise bending moment is $3.5249e^6$ N-m and standard deviation is $6.1818e^6$ N-m. The standard deviation is higher than the mean. This is because of the bending moment due to gravity which changes its sign over one rotation and back. Hence, it's mean will be zero. The edge-wise bending moment's mean comes only from bending moment due to rotation. The maximum edge-wise bending moment is $1.5931e^7$ N-m. Both the mean and maximum are less than flap-wise. But, for one rotation, the bending moment goes from approx. $1e^7$ to $-0.5e^7$. The average cycle has a height of approx. $1.5e^7$. The blade has to be designed to have a structural strength to withstand the fatigue generated due to these cycles for the turbine's designed life.
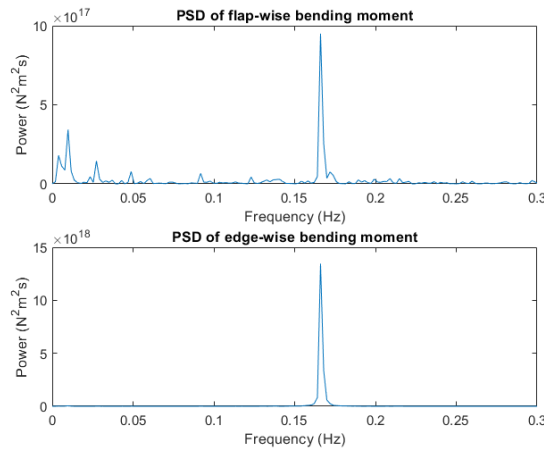

Figure 53: Plot of power spectrum of flap-wise and edge-wise bending moments for blade load case 4

Figure 53 shows the power spectral density (PSD) of flap-wise and edge-wise bending moments plotted without mean. The highest occurs at a frequency of 0.167Hz for both which is the frequency of rotation, 10rpm ($10/60 = 0.167Hz$). For flap-wise, it is due to wind shear and for edge-wise, it is due to gravity. Except at the rotation frequency (1p), the flap-wise bending moment dies out more rapidly than the turbulence. The energy at 3p frequency is not seen because only one blade is considered but not all 3 blades. The PSDs of other blade load cases can be seen in appendix C.
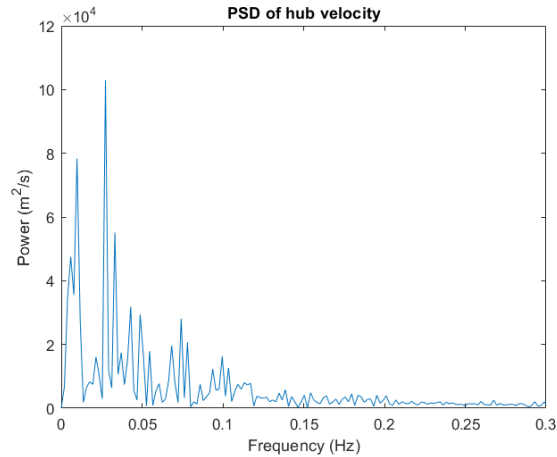

Figure 54: Plot of power spectrum of turbulent wind velocities at hub

Figure 54 shows the PSD of turbulent wind velocities at hub. The effect of turbulence is visible on flap-wise bending moment at low frequencies. Edge-wise bending moment has almost no effect from turbulence because it's energy comes mainly from gravitational force.

The power spectral densities of flap-wise bending moment for all four blade load cases without mean can be seen in figure 55. For blade load case 1, when no shear and turbulence is present, no energy exists at frequencies other than zero which can be seen from figure 55a. For blade load case 2, when shear without turbulence is considered, the energy exists only at frequency 1p which can be seen from figure 55b. For blade load case 3, when turbulence without shear is considered, the energy exists only at frequencies where turbulent kinetic energy is high which can be seen from figure 55c. For blade load case 4, when both shear and turbulence is considered, the energy exists at frequency 1p and at frequencies where turbulent kinetic energy is high which can be seen from figure 55d. Figure 55d is just a linear combination of figures 55b and 55c because the loads on the blade vary almost linearly with wind speed.
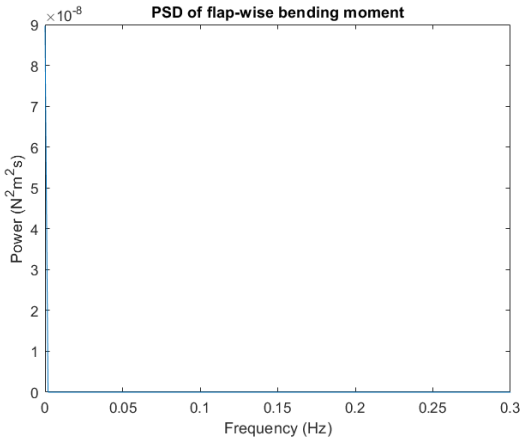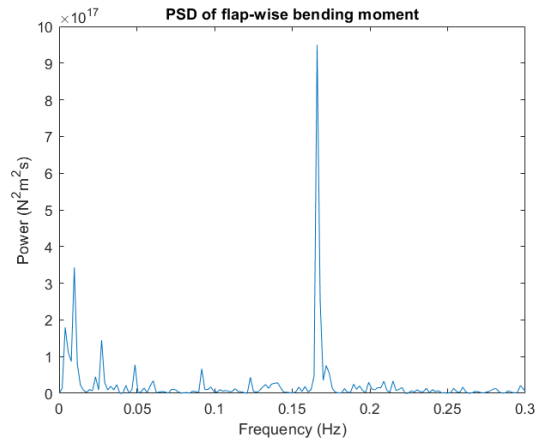
(a) Plot of power spectrum of flap-wise bending moment for blade load case 1
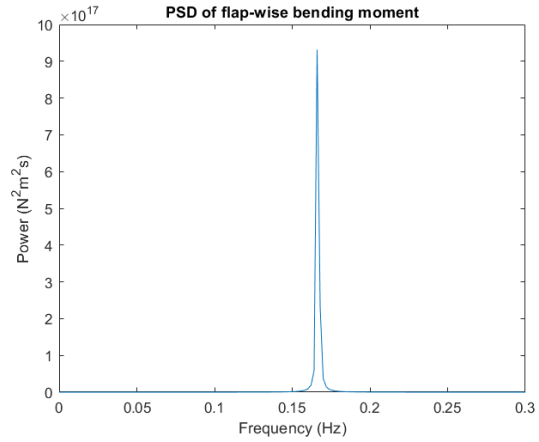
(b) Plot of power spectrum of flap-wise bending moment for blade load case 2
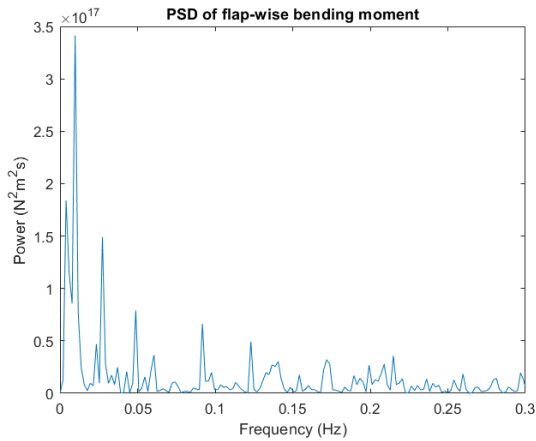
(c) Plot of power spectrum of flap-wise bending moment for blade load case 3

(d) Plot of power spectrum of flap-wise bending moment for blade load case 4

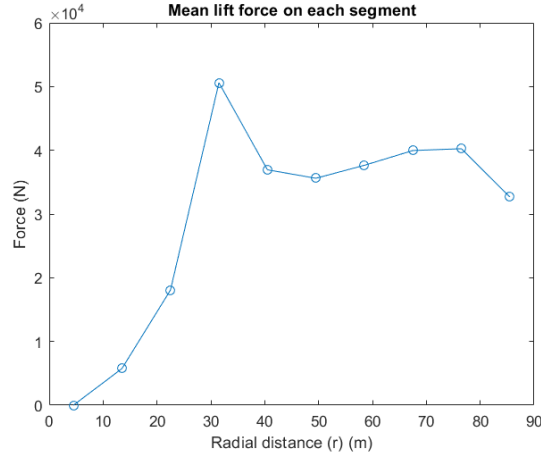Figure 55: Plot of power spectrum of flap-wise bending moments for all four blade load cases

Figure 56: Plot of mean lift force on each segment of the blade for blade load case 4

The mean lift force calculated for all the time steps in general increases radially over the blade and reaches maximum at around 85% of the radius. The higher lift force at inner sections of the blade is due to the increased aerodynamic performance by introduction of Gurney flaps (7). And also due to higher chord length from the design of the blade and high lift coefficient due to blade's pitch angle.
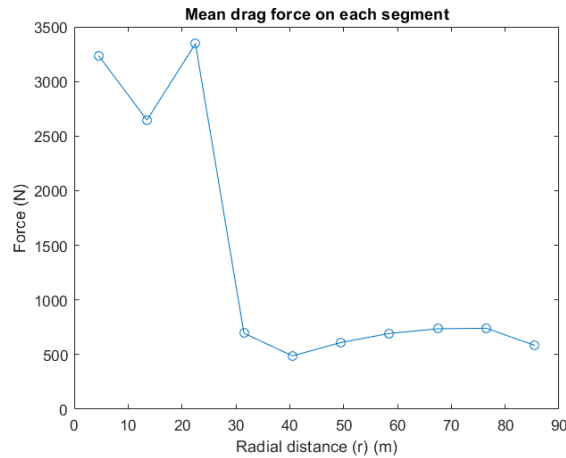

Figure 57: Plot of mean drag force on each segment of the blade for blade load case 4

The drag force in general decreases radially over the blade. The higher drag force at 20m radius is due to higher chord length from the design of the blade.
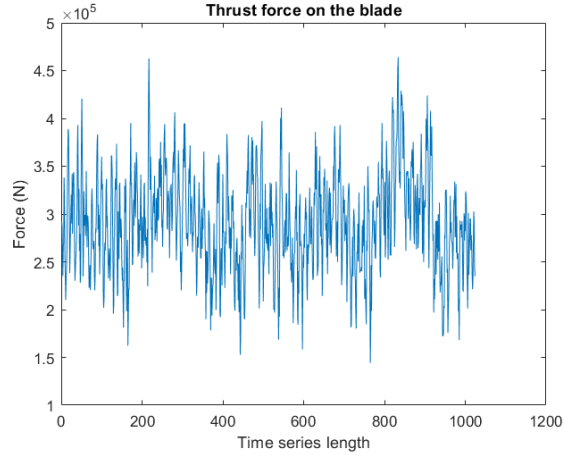
Figure 58: Plot of total thrust force on the blade for blade load case 4

Figure 58 shows the total thrust force on the blade for all the time steps. It can be seen form figure 50 that the flap-wise bending moment is highly coherent with thrust.

3.6.3 High shear and turbulence

In the section 3.6.1, the effect of absence of wind shear and turbulence has been looked at. Now, they are intensified to see if any drastic changes in bending moments occur. A new wind field is created with the following parameters. The shear in the wind profile has increased by increasing the roughness length from 0.01m to 0.1m and turbulent intensity has increased from 10% to 20% [5]. The mean wind speed at hub height is kept constant at 17.7m/s. The new wind profile with 0.1m roughness length is made from U_{hub} and hub height as reference wind speed and height. Three different load cases are investigated. The same turbulent time history is used for all three cases. The results provided are for one realization of the wind field.

Blade load case 5: High wind shear and no turbulence
Blade load case 6: No wind shear and high turbulence
Blade load case 7: High wind shear and high turbulence

---

[5]Average power production has slightly increased due to higher wind speeds but the axial induction factor is not adjusted in BEM theory

Table 13: Bending moments for various cases with high shear and turbulence in N-m

Blade load case	Mean flap-wise bending moment	Maximum flap-wise bending moment	Mean edge-wise bending moment	Maximum edge-wise bending moment	Maximum cycle height edge-wise
5	$1.5593e^7$	$1.8220e^7$	$3.4556e^6$	$1.2191e^7$	$1.7316e^7$
6	$1.5843e^7$	$3.3030e^7$	$3.7300e^6$	$1.7849e^7$	$2.6928e^7$
7	$1.5404e^7$	$3.1695e^7$	$3.6327e^6$	$1.7849e^7$	$2.6928e^7$

Table 14: Standard deviation of bending moments with high shear and turbulence in N-m

Blade load case	Standard deviation flap-wise bending moment	Standard deviation edge-wise bending moment
5	$2.1637e^6$	$6.1601e^6$
6	$5.6708e^6$	$6.3473e^6$
7	$6.0498e^6$	$6.3731e^6$

Comparing load cases 1 and 5 from tables 11 and 13, the magnitude of bending moment values are comparable when shear is increased. High shear has some influence but no drastic changes are observed except for an increase in standard deviation. Comparing load cases 6 and 7 when high turbulence exists, again, lack of shear increases the mean bending moment values slightly. Also introducing shear decreases the maximum flap-wise bending moment by 4% which is contrary from what is observed in section 3.6.1. This might be because of the influence of high turbulence in the wind field. As expected, shear has no influence on maximum edge-wise bending moment. Also, increase in standard deviation for flap-wise by 7% has been observed.

From load cases 1 and 6, only the mean bending moment values are comparable when turbulence is highly increased. High turbulence increases the maximum and standard deviation values drastically. The maximum flap-wise bending moment has been more than doubled, increased by 106%. Maximum edge-wise bending moment has been increased by 45% and maximum cycle height by 55%.

Comparing load cases 5 and 7 when high shear is present, introducing high turbulence decreases the mean flap-wise bending moment (1.5%) and increases the mean edge-wise bending moment (5%) slightly. This is different from section 3.6.1 where turbulence has almost no visible effect on mean values. The maximum flap-wise and edge-wise bending moments increase by 74% and 47% respectively. Also, the standard deviation of flap-wise and edge-wise increase by 180% and 3.5% respectively. Therefore, increasing turbulence in the wind field increases the maximum root bending moments, cycle height and standard deviation of flap-

wise drastically which in turn has a high influence on the blades fatigue life. Plots of bending moments for load cases 5,6 and 7 can be seen in appendix D.

It has also been noticed that the thrust force on the blade for couple of time steps is negative when high turbulence is present. This is because the turbulent velocities at these particular time steps are very high and acting opposite in the mean wind direction. This gives a very low ϕ. Since the blade has some twist and pitch, the angle of attack, α becomes negative. This gives negative lift coefficients and the thrust becomes negative. Figure 59 shows the thrust values for blade load case 7. Even though the thrust on a single blade is negative, the total thrust force on the turbine could be positive acting perpendicular to the rotor plane and in the mean wind direction.
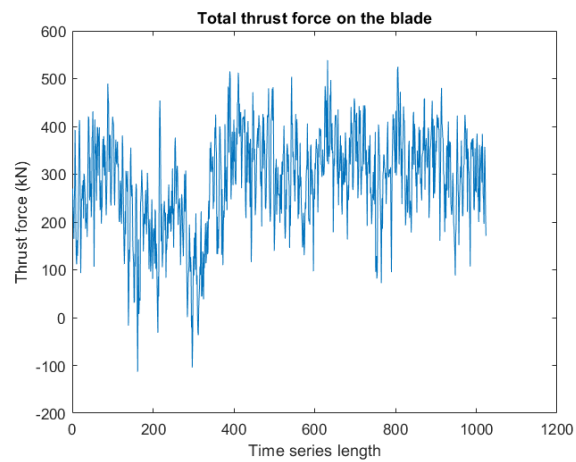
Figure 59: Plot of thrust force for all time steps on a single blade of the HAWT in high shear and high turbulence in kN

Figure 60 shows the wind speeds in the rotor plane for a random time step for both wind fields with low and high turbulence and shear, blade load cases 4 and 7. The color bar on the right side indicates magnitude of wind speeds in m/s. Clearly the wind field with high turbulence and shear has higher magnitudes and variation of wind speeds in the rotor plane. As the blade rotates in this rotor plane over a revolution, it experiences higher variation in bending moment values.
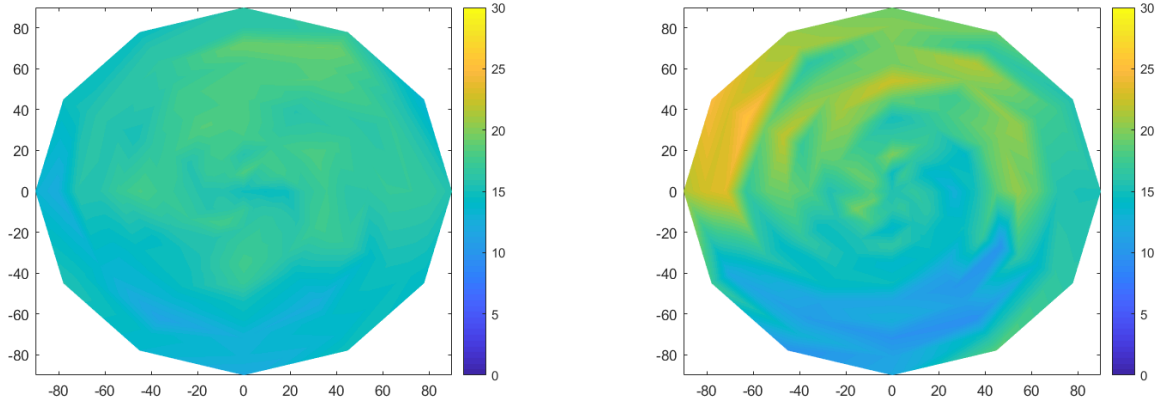
(a) Snapshot of wind field with 10% T.I and 0.01 roughness length

(b) Snapshot of wind field with 20% T.I and 0.1 roughness length

Figure 60: Plot of snapshots of the animated polar wind fields with low and high turbulence and shear. The color bar suggests wind speed in m/s.

3.6.4 Blade load case 4 with high turbulence

It has been observed that turbulence has higher effect on maximum bending moment values than shear. One last comparison has been performed by keeping the shear constant and increasing the turbulence. Blade load case 4 with turbulence intensity (T.I) of 10% and roughness length of 0.01m has been taken. A new wind field is created with 20% turbulence intensity but with same roughness length of 0.01m and compared.

Table 15: Maximum (max) and standard deviation (std) of bending moments with 10% and 20% T.I in N-m

T.I	Max flap-wise	Std flap-wise	Max edge-wise	Std flap-wise
10%	$2.5811e^7$	$2.9499e^6$	$1.5931e^7$	$6.1818e^6$
20%	$3.2204e^7$	$5.5434e^6$	$1.7902e^7$	$6.4146e^6$

Comparing T.I of 20% with 10%, the maximum and std of flap-wise bending moment has increased by 25% and 88% respectively. The increment in standard deviation is almost proportional to the increment in T.I. The maximum and std of edge-wise bending moment has increased by 13% and 4% respectively. So, doubling the turbulence in the wind field with same shear increases maximum flap-wise bending moment by 25% and also the standard deviation by 88% which will have a lot of effect on maximum and fatigue load cases.
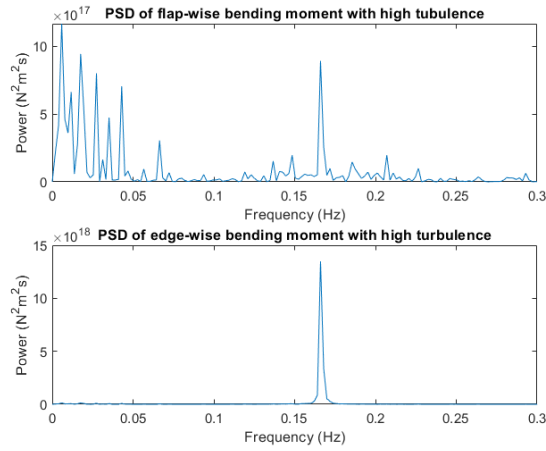
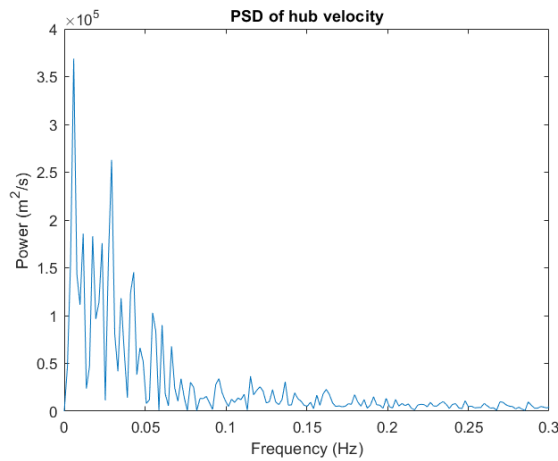Figure 61: Plot of power spectrum of flap-wise and edge-wise bending moments for T.I of 20%

Figure 62: Plot of power spectrum of turbulent wind velocities at hub for T.I of 20%

Comparing the Fourier analysis of bending moments from wind fields with 10% and 20% T.I, from figures 53 and 61, the maximum energy no longer occurs at the rotational frequency of the turbine (0.167Hz) for flap-wise bending moment when high turbulence is present. It occurs at frequencies where maximum turbulent kinetic energy happens. Figure 62 shows the spectral density of turbulent wind velocities at hub for wind field with 20% T.I. Comparing with figure 54, many low frequencies with high turbulent kinetic energy exists when T.I is higher.

4   Conclusion

Two measured signals from FINO1 platform at 40m and 80m height are tested by Sandia method to see if they can be reproduced back. It has been observed that, Sandia method applied as it is, can reproduce the first signal exactly but gives higher standard deviation for the second signal. If random phases are used instead of it's own phases in generation of second time series, same standard deviation can be achieved. The method depends on randomness in phase generation. If no information about second time series is available, a theoretical coherence function, same spectra as first/input time series and random phases can be used for it's generation. But, this procedure gives almost same statistics as the input signal for second signal. A slight increment in standard deviation is observed.

The above procedure cannot be applied explicitly. If a second time series is generated by Sandia method, it is not wise to use the phase angles of the generated time series to create a third time series but rather use the same random phase angles used to create the second time series as input for third time series generation.

Based on Sandia method, codes for generation of wind fields have been developed. Both rectangular and polar wind fields have been created but proceeded with polar wind field due to it's easy practicality with Horizontal Axis Wind Turbines. A different way of plotting coherence has also been looked at. Concatenated coherence represents the original coherence better than the averaged coherence because of reduction in margin of error.

The difference in root bending moment values of the blade based on variation in shear and turbulence in the wind field has been investigated. It has been observed that, shear has more influence on mean bending moment and turbulence on max bending moment. The magnitude of influence of shear on mean is small compared to turbulence on maximum but not negligible. Both shear and turbulence has an effect on standard deviation of root bending moments but the effect of turbulence is larger.

The effect of turbulence on maximum and standard deviation of bending moments has been looked further by increasing the turbulence intensity (T.I) from 10% to 20% in the wind field with 0.01m roughness length. The maximum flap-wise bending moment increases by 25% and standard deviation by 88%. The Fourier analysis of flap-wise bending moment shows that the frequency that contains most energy has been shifted from rotational frequency of the turbine (for 10% T.I) to the frequencies where turbulent kinetic energy is high (for 20% T.I).

In short, a change in turbulence in the wind field will have a drastic change on ultimate limit state and fatigue limit state design load cases. So, it is highly important to get the turbulence right. This again depends on getting the right coherence in generation of the wind field. Again, Sandia method gives a little increment in standard deviation (turbulence) of the generated time series. This will have an effect on maximum and standard deviation of root bending moments of the blade of the wind turbine.

5 Further study

- Sandia method can be checked for longer time series to see the difference in the statistics of the re-generated signals and for more than 2 measured signals to see the effect of previous signals spectra and phase angles in re-generating new one

- Various coherence models can be implemented in the wind field generation and the statistics and coherence of these different wind fields can be compared

- When generating a wind field based on Sandia method, different auto-spectra can be used on the diagonal of spectral matrix based on different points in the wind field at various locations

- Phase lag of turbulent eddies due to variation of mean wind speed at various heights in the atmosphere can be implemented while generating a wind field

- The bending moment values at the root of the blade that are computed in this thesis are only for one realization of a wind field. The difference in these values can be checked for many realizations while using the same parameters for wind fields generation

- The wind fields that are developed is for above rated wind speed of DTU 10MW wind turbine. Wind fields with below rated wind speed at hub can be generated and compared with above rated to see if a similar pattern in loads is followed

- Tip losses, Glautert limit and 3D effects can be implemented in BEM theory while calculating loads on the turbine

References

[1] Roland B. Stull. *An Introduction to Boundary Layer Meteorology*, pages 115–149. 01 1988. ISBN 978-90-277-2769-5. doi: 10.1007/978-94-009-3027-8_4.

[2] Sergio González Horcas, François Debrabandere, Benoît Tartinville, Charles Hirsch, and Grégory Coussement. *CFD Study of DTU 10 MW RWT Aeroelasticity and Rotor-Tower Interactions*, pages 309–334. Springer International Publishing, Cham, 2016. ISBN 978-3-319-39095-6. doi: 10.1007/978-3-319-39095-6_18. URL https://doi.org/10.1007/978-3-319-39095-6_18.

[3] Richard Crossley and Peter J. Schubel. Wind turbine blade design. *Energies*, 5, 09 2012. doi: 10.3390/en5093425.

[4] Olivier Cleynen. Airfoil nomenclature, April 2011. URL https://commons.wikimedia.org/wiki/File:Wing_profile_nomenclature.svg.

[5] M.O.L. Hansen. Aerodynamics of wind turbines: Third edition. *Aerodynamics of Wind Turbines: Third Edition*, pages 1–173, 01 2015. doi: 10.4324/9781315769981.

[6] Hamid M Sedighi, Kourosh Heidari Shirazi, and Jamal Zare. Novel equivalent function for deadzone nonlinearity: Applied to analytical solution of beam vibration using he's parameter expanding method. *Latin American Journal of Solids and Structures*, 9: 443–451, 10 2012. doi: 10.1590/S1679-78252012000400002.

[7] Christian Bak, Frederik Zahle, Robert Bitsche, Taeseong Kim, Anders Yde, Lars C. Henriksen, Anand Natarajan, and Morten Hansen. *Description of the DTU 10 MW Reference Wind Turbine, Report Number: DTU Wind Energy Report-I-0092.* 06 2013.

[8] Paul Veers. Three-dimensional wind simulation, sandia national laboratories, sand88-0152. 01 1988.

[9] Jakob Mann. Wind field simulation. *Probabilistic Engineering Mechanics*, 13(4):269 – 282, 1998. ISSN 0266-8920. doi: https://doi.org/10.1016/S0266-8920(97)00036-2. URL http://www.sciencedirect.com/science/article/pii/S0266892097000362.

[10] Korn Saranyasoontorn, Lance Manuel, and Paul Veers. A comparison of standard coherence models for inflow turbulence with estimates from field measurements [11]. *Journal of Solar Energy Engineering*, 126:1069–1082, 11 2004. doi: 10.1115/1.1797978.

[11] A Chougule, J Mann, and M Kelly. Vertical cross-spectral phases in atmospheric flow. *Journal of Physics: Conference Series*, 555:012017, nov 2014. doi: 10.1088/1742-6596/555/1/012017. URL https://doi.org/10.1088%2F1742-6596%2F555%2F1%2F012017.

[12] M. Shinozuka and C.-M. Jan. Digital simulation of random processes and its applications. *Journal of Sound and Vibration*, 25(1):111 – 128, 1972. ISSN 0022-460X. doi:

https://doi.org/10.1016/0022-460X(72)90600-1. URL `http://www.sciencedirect.com/science/article/pii/0022460X72906001`.

[13] W Frost, B H. Long, and R E. Turner. Engineering handbook on the atmospheric environmental guidelines for use in wind turbine generator development. 12 1978.

[14] A Nybø, F G Nielsen, and J Reuder. Processing of sonic anemometer measurements for offshore wind turbine applications.

[15] Matlab. Mean squared coherence. URL `https://se.mathworks.com/help/signal/ref/mscohere.html`.

[16] Junbo Jia, R Ellefsen, and Tore Holmas. Practical fatigue calculation for offshore structures based on efficient wave spectrum inputs. *Proceedings of the International Offshore and Polar Engineering Conference*, pages 310–317, 01 2008.

[17] Lene Eliassen and Charlotte Obhrai. Coherence of turbulent wind under neutral wind conditions at fino1. *Energy Procedia*, 94:388–398, 09 2016. doi: 10.1016/j.egypro.2016.09.199.

[18] Statistics How To. Margin of error. URL `https://www.statisticshowto.datasciencecentral.com/probability-and-statistics/hypothesis-testing/margin-of-error/`.

[19] Dehghan, Manshadi, and Mojtaba. *The Importance of Turbulence Reduction in Assessment of Wind Tunnel Flow Quality*. 07 2011. ISBN 978-953-307-623-2. doi: 10.5772/17069.

Appendix

A   Matlab code for Polar wind field generation

```matlab
% Polar wind field based on Sandia Method

% xxxxxxxxxxxxxxx INPUT DATA
    xxxxxxxxxxxxxxxxxxxxxxxxxxxxxxxxxxxxxxxxx
x = importdata('Timeseries_at_hub_height.txt');

dt = 0.5; % timestep
m = 21; %No of points along Y axis and same on Z-axis
dy = 9; %distance between each point along Y axis
dz = 9; %distance between each point along Y axis
U = 13.6; % Mean wind velocity at hub height
u_10 = 10; %Mean wind velocity at 10m height (if different height,
    have to modify in power law)
Z0 = 0.01; % roughness length
h = 120; % hub height
r = 90; % rotor radius
w = pi/6; % For 12 no. of points in a circle
% xxxxxxxxxxxxxxxxxxxxxxxxxxxxxxxxxxxxxxxxxxxxxxxxxxxxxxxxxxxxxxxxxxxx

N = length(x); %length of the time series
fs = 1/dt; %Sampling frequency
f = (0:fs/N:fs/2)'; %frequency scale til Nyquist frequency
T = N*dt; %Total time
t = 0:dt:T-dt; %time scale
theta = 0:w:2*pi-w; % angle for each point in a circle
n = (((m-1)/2)*length(theta))+1; % Total no. of points in the
    polar wind field including
                                  % hub point (origin)

% Re-constructing signal by Coherence and phase information

% Polar Co-ordinates for distance in coherence fuction
%The origin is at hub and going counter clockwise at each dy
YZ = zeros(n,1);
k = 1;
for i = 1:(m-1)/2
    for j = 1:length(theta)
        k = k+1;
```

```matlab
36            YZ(k) = i*dz*exp(1i*theta(j));
37        end
38  end
39
40  plot(YZ)
41
42  % Performing fft of original signal to get auto spectrum and phase
           information
43  X = fft(x);
44  Pxx = abs(X(1:(N/2)+1)).^2;
45  phaseX = angle(X(1:(N/2)+1));
46
47  % Definining Spectral Matrix 'S'
48  % Diagonal of spectral matrix
49  S = zeros(n,n,(N/2)+1);
50  for i=1:n
51      S(i,i,:) = Pxx; %PSD of diagonal (Assumed same as x !!)
52  end
53
54  % Other elements of spectral matrix by theoritical coherence
         function with decay coeff 7.5
55  p = 1;
56  for i=2:n
57      for j=1:i-1
58            Coh(:,p) = exp(-7.5*abs(YZ(i)-YZ(j))*f/U);
59            a = reshape(sqrt(S(i,i,:).*S(j,j,:)),[],1);
60            S(i,j,:) = Coh(:,p).*a; % Cross spectral matrix based on
                 theoritical coherence
61            S(j,i,:) = S(i,j,:);
62            p=p+1;
63      end
64  end
65
66  % Defining Phase information
67  phase = zeros(length(phaseX),n-1);
68  phase = [phaseX phase]; % Phase matrix for all points
69
70  % Defining Transformation Matrix 'H' and fourier coefficients
       matrix 'V'
71  H = zeros(size(S));
72  V = zeros((N/2)+1,n);
73  H(1,1,:) = sqrt(S(1,1,:));
```

```matlab
V(:,1) = reshape(H(1,1,:),[],1).*exp(1i*phase(:,1));
for j = 2:n
    phase(:,j) = -pi+2*pi*rand((N/2)+1,1); %Uniformly distributed
        random phase between 0 to 2pi
    a = 0;
    for k = 1:j
        if k~=j
            p=0;
            for l = 1:k-1
                p = p + (H(j,l,:).*H(k,l,:));
            end
            H(j,k,:) = (S(j,k,:)-p)./H(k,k,:);
        else
            q=0;
            for l = 1:k-1
                q = q + (H(k,l,:).*H(k,l,:));
            end
            H(k,k,:) = sqrt(S(k,k,:)-q);
        end
        H(isnan(H))=0;
        a = a + reshape(H(j,k,:),[],1).*exp(1i*phase(:,k));
    end
    V(:,j) = a;
    %phase(:,j) = angle(V(:,j));
end

% Constructing time series from 'V'
v = zeros(N,n);
for j = 1:n
    v(:,j) = real(2*ifft(V(:,j),N));
end

%writing velocities and polar co-ordinates to a text file
dlmwrite('turbulent_velocities_at_each_point_Sandia_polar.txt',v,'
    precision','%.4f','delimiter','\t')
dlmwrite('polar_coordinates_at_each_point_Sandia_polar.txt',YZ,'
    precision','%.4f','delimiter','\t')
```

B   Beam load cases 1 and 2 with rotation

Beam load case 1 - Homogeneous wind field
Beam load case 2 - Steady wind field

Table 16: Bending moment values for load cases 1 and 2 with rotation

Load case	Mean	Maximum
1	$1.9163e^7$	$1.9163e^7$
2	$1.9143e^7$	$1.9272e^7$

Plots for the bending moment, drag force along the beam for a random time step and drag force variability for segment 1 and segment 10 are shown only for load case 2 since there won't be any variability for load case 1 with rotation. It can be seen that the bending moment and shear forces vary with a frequency of 1p.
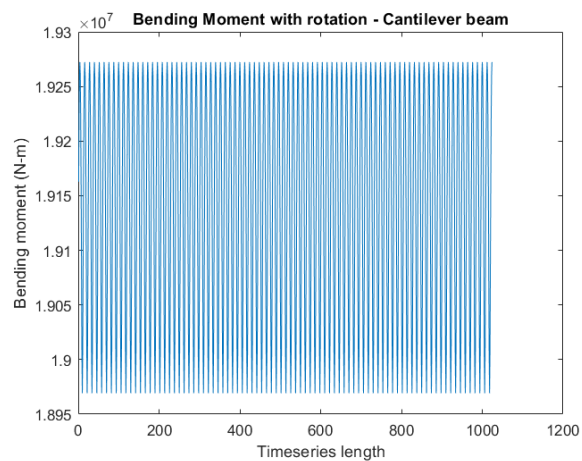
Figure 63: Plot of root bending moment of the beam placed in the polar wind field for load case 2 with rotation
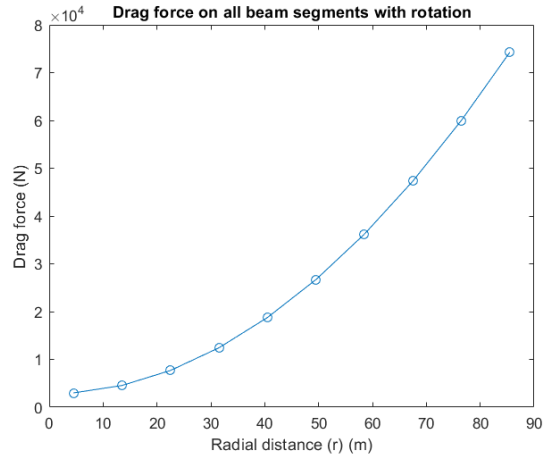
Figure 64: Plot of drag forces on the beam at each segment for a random time step for load case 2 with rotation
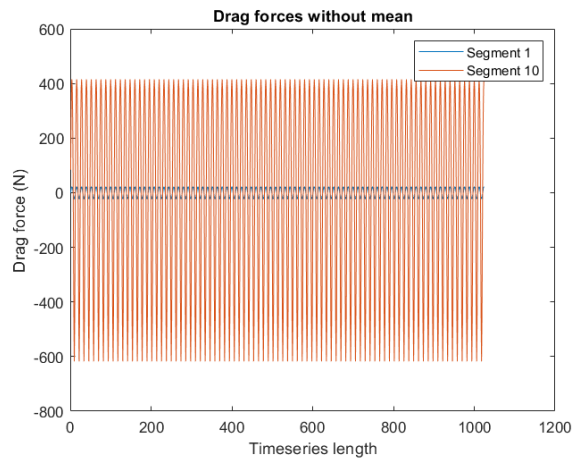
Figure 65: Plot of drag force variability on the beam at segment 1 and segment 10 for load case 2 with rotation

74

C Plots of bending moments and forces for blade load cases 1, 2 and 3

C.1 Blade load case 1 - No shear and no turbulence
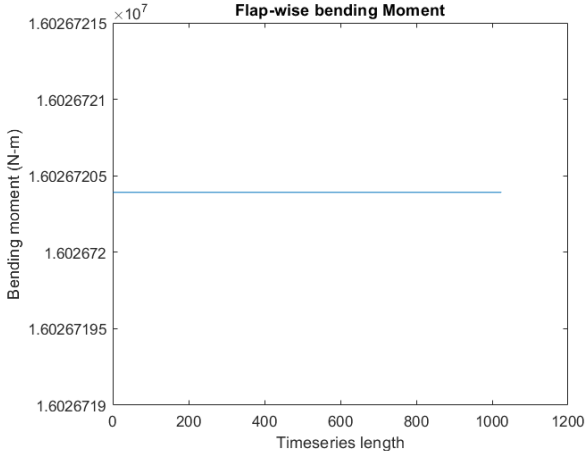
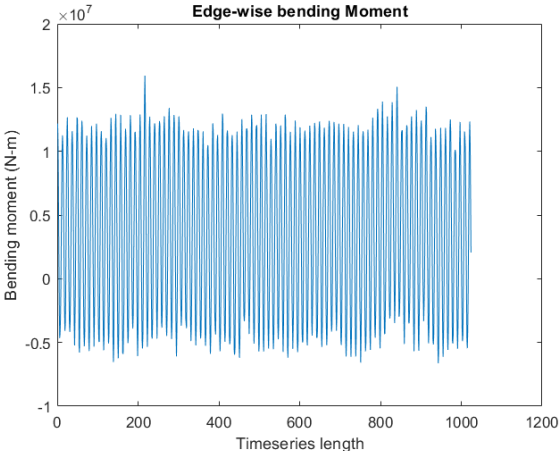Figure 66: Plot of flap-wise bending moment for blade load case 1
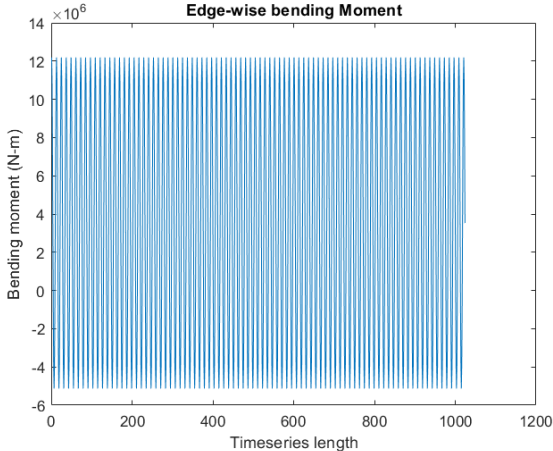
Figure 67: Plot of edge-wise bending moment for blade load case 1
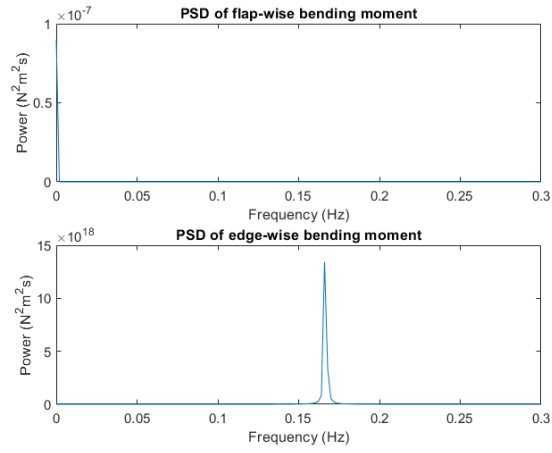
Figure 68: Plot of power spectrum of bending moments for blade load case 1
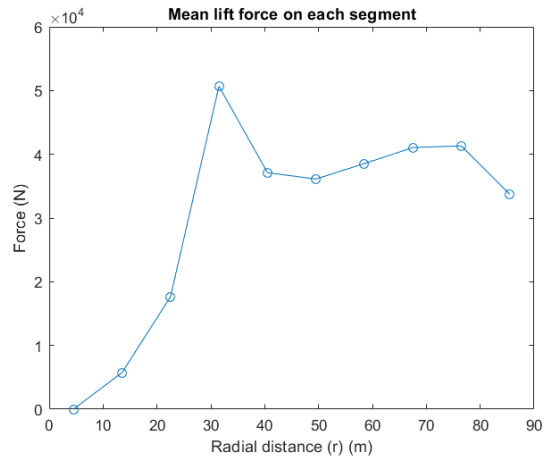
Figure 69: Plot of mean lift force on each segment of the blade for blade load case 1
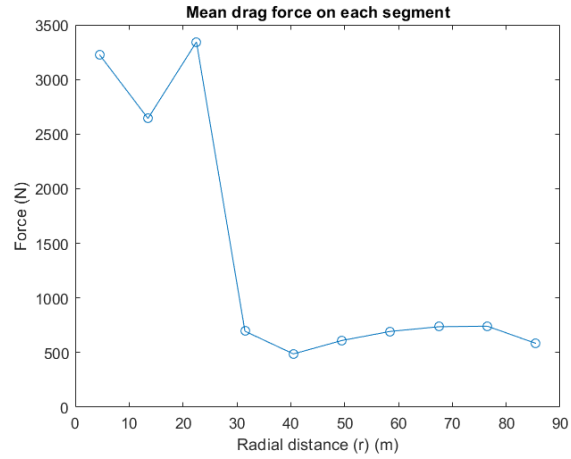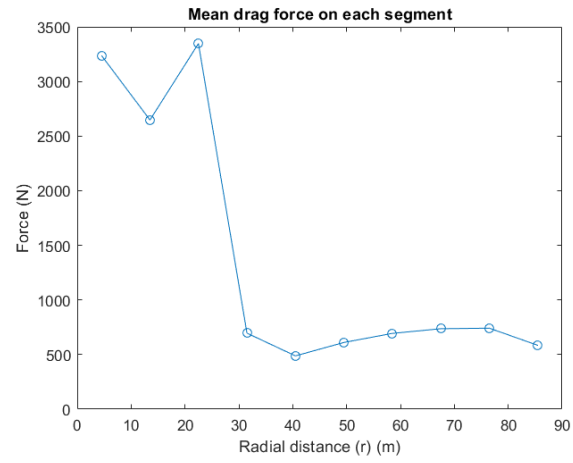
Figure 70: Plot of mean drag force on each segment of the blade for load case 1

C.2   Blade load case 2 - with shear and no turbulence
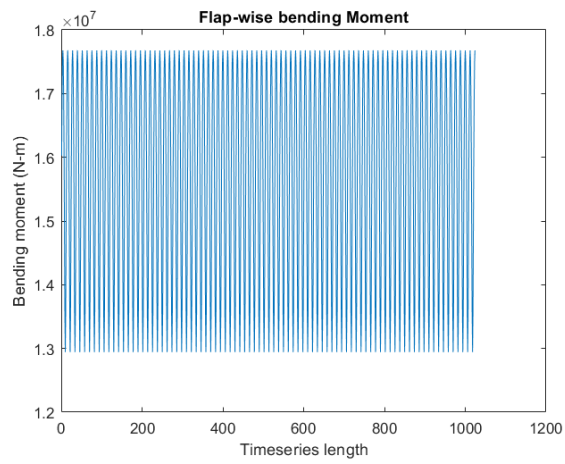
Figure 71: Plot of flap-wise bending moment for blade load case 2
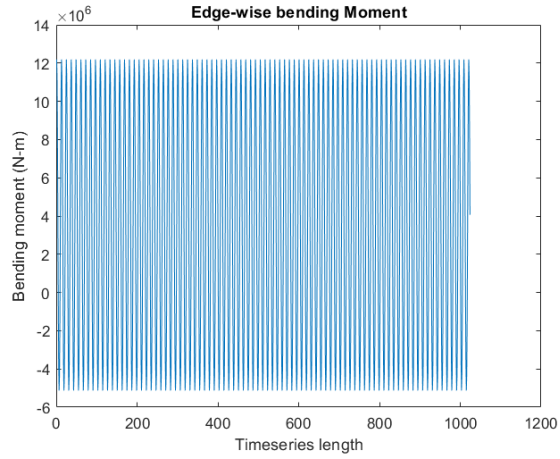
Figure 72: Plot of edge-wise bending moment for blade load case 2
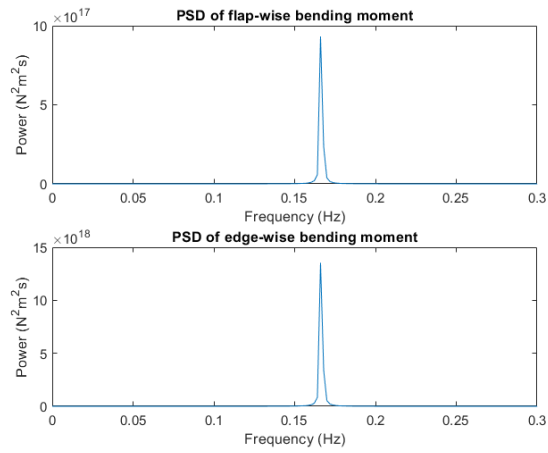
Figure 73: Plot of power spectrum of bending moments for blade load case 2
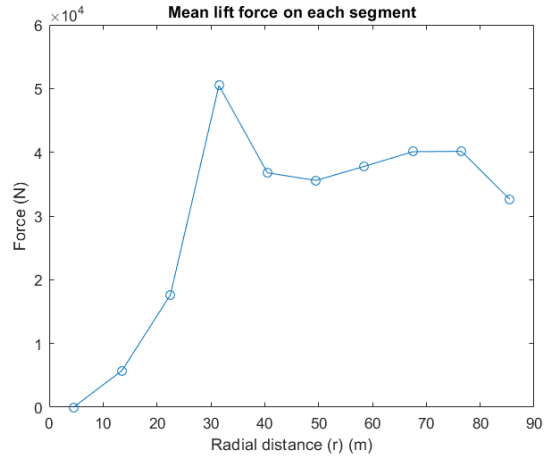
Figure 74: Plot of mean lift force on each segment of the blade for blade load case 2
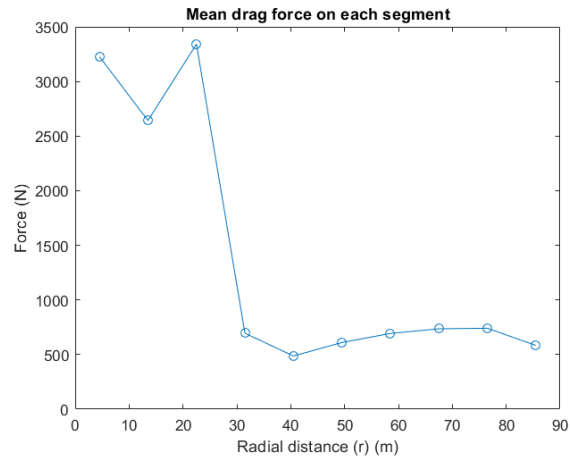
Figure 75: Plot of mean drag force on each segment of the blade for load case 2

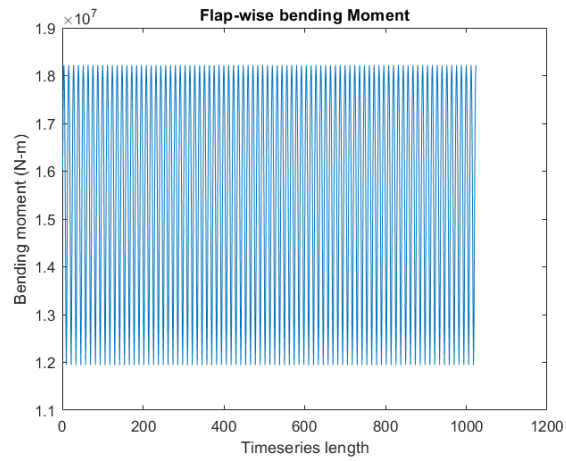## C.3 Blade load case 3 - no shear and with turbulence
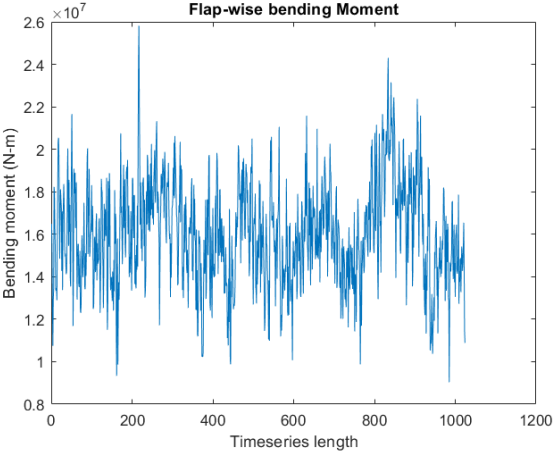
Figure 76: Plot of flap-wise bending moment for blade load case 3

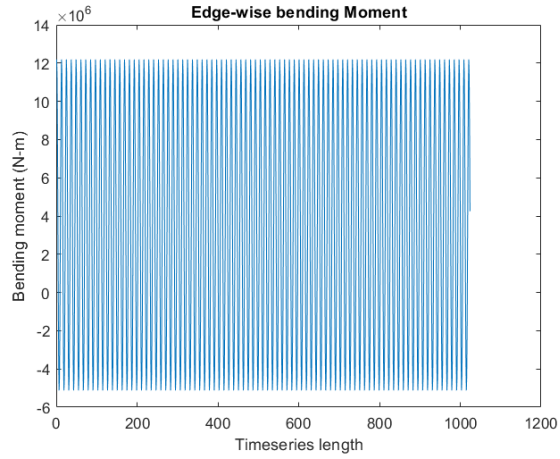

Figure 77: Plot of edge-wise bending moment for blade load case 3
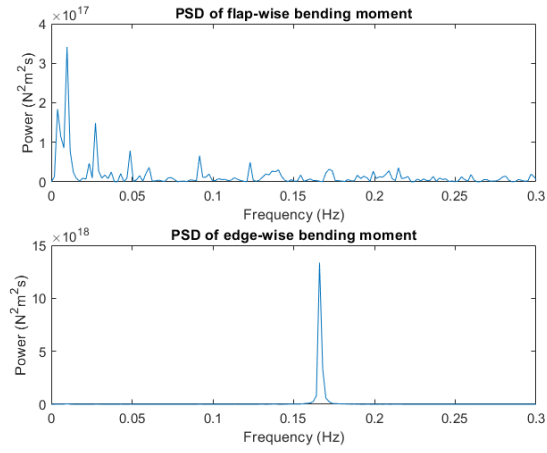
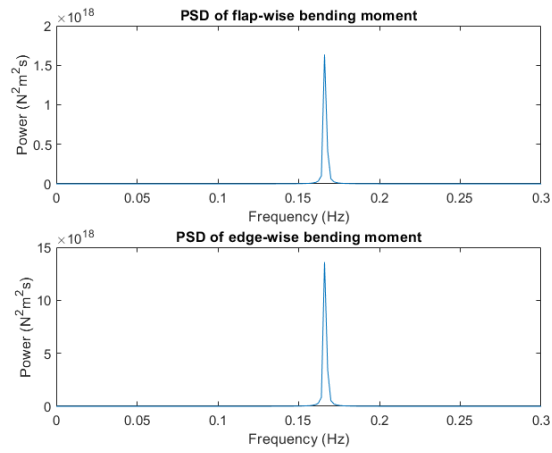Figure 78: Plot of power spectrum of bending moments for blade load case 3
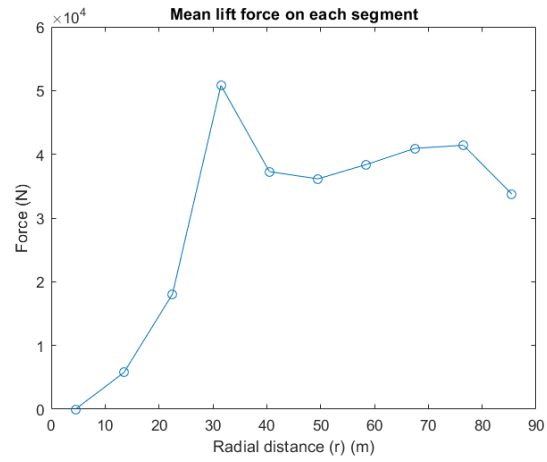
Figure 79: Plot of mean lift force on each segment of the blade for blade load case 3

Figure 80: Plot of mean drag force on each segment of the blade for load case 3

D Plots of bending moments for high shear and turbulence load cases

Blade load case 5: High wind shear and no turbulence
Blade load case 6: No wind shear and high turbulence
Blade load case 7: High wind shear and high turbulence

D.1 Initial time series of turbulent wind velocities at hub

The time series of wind velocities used to generate the polar wind field with high shear and turbulence is plotted below. This time series is initially generated in Qblade software. This is the initial time series for all the above blade load cases
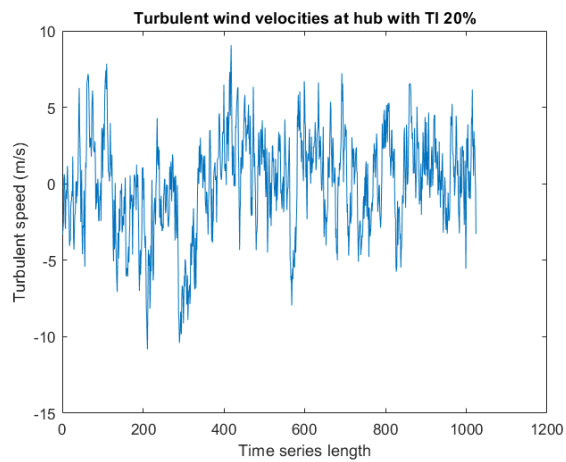
Figure 81: Plot of initial time series with high turbulence and shear
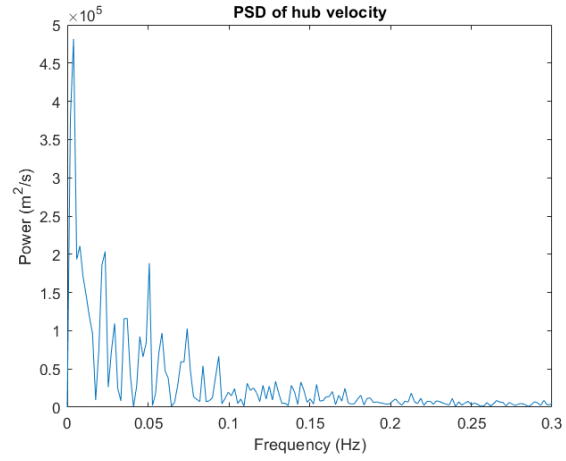
Figure 82: Plot of power spectrum of initial time series at hub

D.2 Blade load case 5

Figure 83: Plot of flap-wise bending moment for blade load case 5

Figure 84: Plot of edge-wise bending moment for blade load case 5

Figure 85: Plot of power spectrum of bending moments for blade load case 4
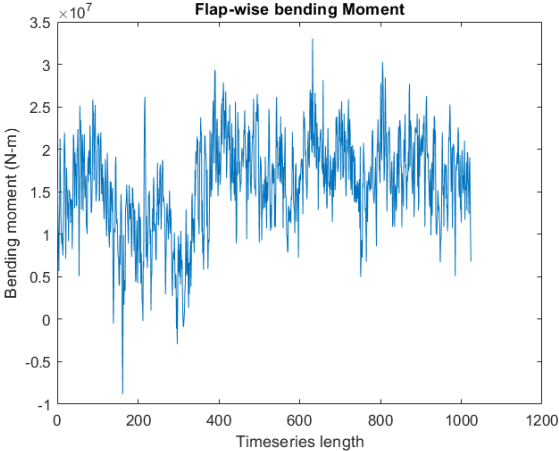
D.3 Blade load case 6

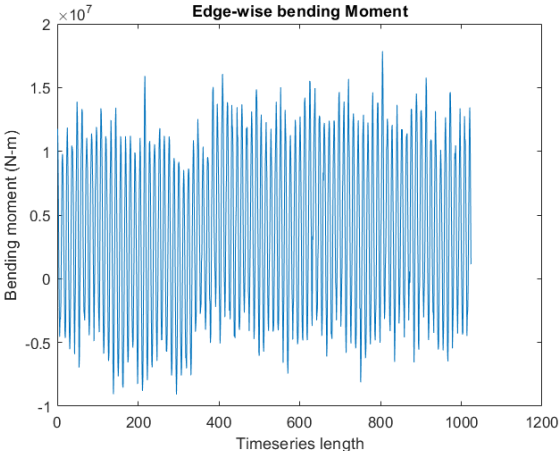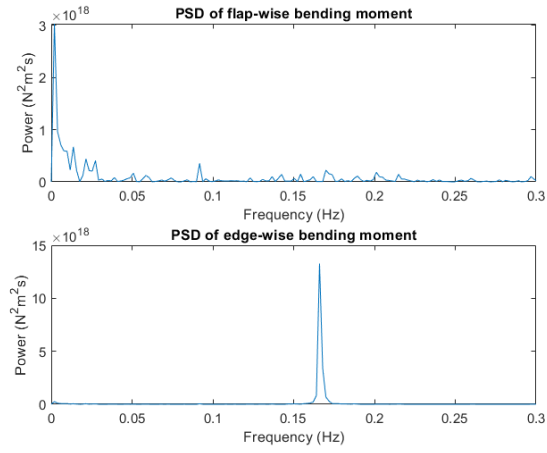Figure 86: Plot of flap-wise bending moment for blade load case 6

Figure 87: Plot of edge-wise bending moment for blade load case 6

Figure 88: Plot of power spectrum of bending moments for blade load case 6
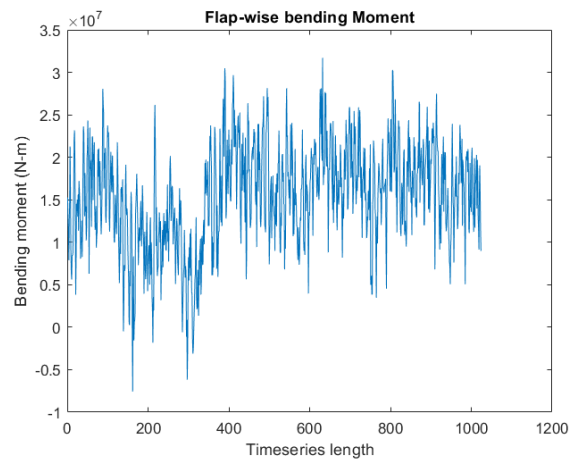
D.4   Blade load case 7

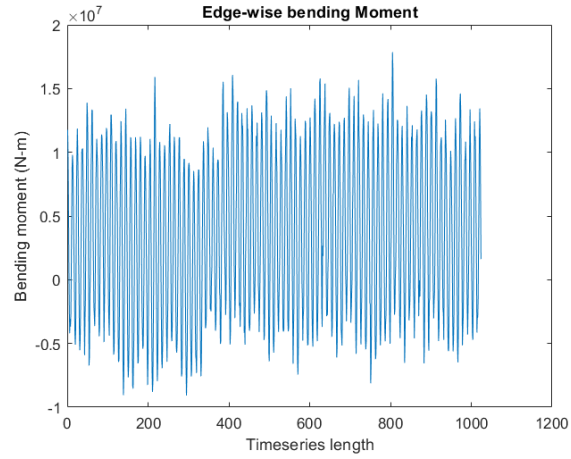Figure 89: Plot of flap-wise bending moment for blade load case 7

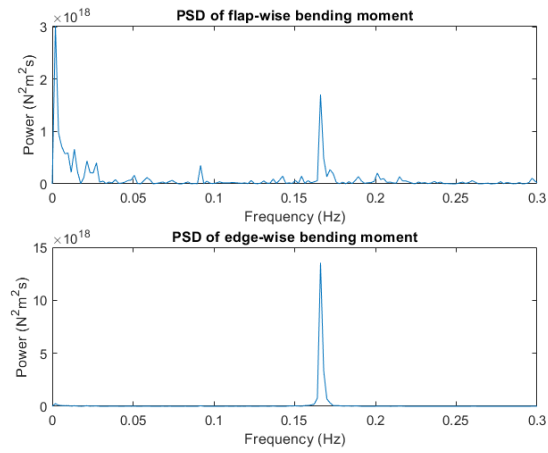Figure 90: Plot of edge-wise bending moment for blade load case 7

Figure 91: Plot of power spectrum of bending moments for blade load case 7